

# An implicit unified gas-kinetic scheme for unsteady flow in all Knudsen regimes



Yajun Zhu<sup>a</sup>, Chengwen Zhong<sup>a</sup>, Kun Xu<sup>b,c,\*</sup>

<sup>a</sup> National Key Laboratory of Science and Technology on Aerodynamic Design and Research, Northwestern Polytechnical University, Xi'an, Shaanxi 710072, China

<sup>b</sup> Department of Mathematics, Hong Kong University of Science and Technology, Hong Kong, China

<sup>c</sup> HKUST Shenzhen Research Institute, Shenzhen 518057, China

## ARTICLE INFO

### Article history:

Received 6 January 2018

Received in revised form 11 December 2018

Accepted 11 January 2019

Available online 26 February 2019

### Keywords:

Unified gas-kinetic scheme

Implicit method

Unsteady flow

Multiscale transport

## ABSTRACT

The unified gas-kinetic scheme (UGKS) is a direct modeling method for multiple scale transport. Based on the ratio of time step to the particle collision time, the local evolution solution on the mesh size and time step scales is used in the construction of the multiscale method. For a flow problem covering multiple flow regimes, such as the hypersonic flow around a flying vehicle in near space, the UGKS is able to capture the highly compressed Navier-Stokes solution in one region and fully expanded free molecular flow in another region, with significant variations of the ratio between the time step and the local particle collision time around the vehicle. For an explicit UGKS, the time step in the whole computational domain is determined by the CFL condition. With implicit and multigrid techniques, the efficiency of the UGKS [1,2] has been improved by two orders of magnitude for steady state computation. However, for unsteady flow computation, due to the CFL condition the global time step used in the explicit UGKS may be limited by the smallest cell size in the computational domain. As a result, for a largely stretched non-uniform mesh the global time step becomes very small and the ratio of the time step to the local particle collision time may get a very small value. Under such a circumstance, even though the UGKS is a multiscale method, the real physics represented in the explicit UGKS may be constrained to the kinetic scale transport only, and the advantage of the multiscale nature in UGKS has not been fully utilized. In order to solve the multiscale unsteady flow problem efficiently, the time step restriction from a global CFL condition has to be released. In this paper, we will develop an implicit UGKS (IUGKS) for unsteady flows by alternatively solving the macroscopic and microscopic governing equations within a time step iteratively. With a pre-defined uniform large evolution time step, the local CFL number varies greatly in different region, such as on the order 1 in the large numerical cell size region, and 100 in the small cell size region. In order to preserve coherent flow evolution and keep the multiscale nature, the time averaged numerical flux across a cell interface is still evaluated by the explicit UGKS under the local CFL condition. Therefore, the multiscale property of the UGKS modeling has been kept over non-uniform meshes. With improved temporal discretization, the current IUGKS can automatically go back to the explicit UGKS and obtain identical solutions when the time step of the implicit scheme gets to that of an explicit one. Many numerical examples are included to validate the scheme for both continuum and rarefied flows with a large variation of artificially generated mesh size. The IUGKS has a second order accuracy and presents reasonably good results for unsteady flow

\* Corresponding author at: Department of Mathematics, Hong Kong University of Science and Technology, Hong Kong, China.

E-mail addresses: zhuyajun@mail.nwpu.edu.cn (Y. Zhu), zhongcw@nwpu.edu.cn (C. Zhong), makxu@ust.hk (K. Xu).

computation, and its efficiency has been improved by dozens of times in comparison with the explicit UGKS.

© 2019 Elsevier Inc. All rights reserved.

## 1. Introduction

The Boltzmann equation is the fundamental governing equation for the molecular gas dynamics on the microscopic level. It has a wide range of applications in many areas, such as rarefied gas flow, photon transport, radiative heat transfer, porous media, and plasma. The modeling scale of the Boltzmann equation is the mean free path and the mean collision time, which gives detailed description of molecular transport. The Boltzmann equation is considered to be valid in all Knudsen number regimes, but with the resolved dynamics down to the mean free path scale everywhere.

The numerical methods starting from the Boltzmann equation or the simplified kinetic model equations include the particle based direct simulation Monte Carlo (DSMC) method [3] and the discrete distribution function based kinetic methods, such as the discrete velocity method (DVM) [4,5], the gas kinetic unified algorithm (GKUA) [6,7], and the unified and discrete unified gas-kinetic schemes (UGKS, DUGKS). For numerical scheme with separate treatment of particle transport and collision, it is always required to resolve the mean free path and mean collision time scale in order to reduce the time-step-dependent numerical dissipation. This requirement severely constrains the cell size and time step used by these schemes in near continuum flow computations. In recent years, the newly developed UGKS [8–10] and DUGKS [11,12] are truly multiscale methods which are capable of capturing non-equilibrium flow physics in all Knudsen number regimes efficiently.

Distinguished from most kinetic methods, such as the DSMC and many DVMs, where operator splitting is used to separately discretize the particle's free transport and collision, the UGKS models the flow physics on the mesh size and time step scales through coupled particle transport and collision within a time step by the integral solution of kinetic model equation. The integral solution covers the flow regime from the particle transport to the hydrodynamic wave evolution. In UGKS, the ratio of time step to the particle mean collision time ( $\Delta t/\tau$ ) identifies the continuum ( $\Delta t/\tau \gg 1$ ) and rarefied ( $\Delta t/\tau \sim 1$ ) flow regime. This ratio can be varied by several orders of magnitude continuously over the whole computational domain in a realistic flow simulation, such as the hypersonic flight in the near space environment. The time step and cell size in UGKS are not constrained by the collision time and particle mean free path [13], which makes the UGKS very efficient in the near continuum flow computation. Different from the gas-kinetic scheme (GKS) [14] with the update of macroscopic flow variables only for the continuum flow computations, the UGKS updates both macroscopic flow variables and microscopic gas distribution function for the capturing of peculiar non-equilibrium gas distribution function. The unified treatment of continuum and rarefied flow physics makes UGKS be suitable for multiscale flow simulations, such as the studies of hypersonic [15,16], rarefied [17], and micro flows [18,19]. At the same time, the methodology of direct modeling [10,20] has been extended to solve other multiscale transport problems, such as plasma [21], radiative transfer [22], and phonon heat transfer [23].

For unsteady flow computation the current explicit UGKS uses a uniform time step which is determined by the Courant-Friedrichs-Lewy (CFL) condition, and the smallest cell size may determine the global time step, such as the time step from cells around the tip of a wing. For high speed flow simulation with significant variation of local cell size, the overall uniform time step can become very small, and it may go to the order of local particle collision time  $\tau$  everywhere. As a result, for unsteady flow computation the multiscale property of UGKS is not fully utilized, even though a much large cell size is used for the near equilibrium regime far away from the flying vehicle. In order to improve the efficiency and keep a reasonable accuracy for unsteady flow computation, it is preferred to develop an implicit UGKS (IUGKS), which releases the constraint of a global CFL condition and preserves the multiscale nature of UGKS in different flow regimes.

The implicit schemes to solve the unsteady Navier-Stokes (NS) equations have been developed using dual-time stepping methods [24–26]. Recently, the time-accurate implicit GKS has also been constructed [27,28] to accelerate computational efficiency for high-speed unsteady and turbulent flows. For rarefied flows, one main problem for the kinetic solvers is about the treatment of the collision term. The implicit scheme in [29] employed a lagged equilibrium state, i.e., using an explicit gain term and an implicit loss term. The implicit GKUA [7] and the early implicit UGKS [30] followed the similar treatment. As analyzed by Mieussens [4,5], the convergence of the implicit schemes may slow down considerably if the gain term and loss term are evaluated at different time levels. Therefore, a linear mapping between the equilibrium state and the gas distribution function was adopted in the discretization of the implicit collision term. In the explicit UGKS and some other asymptotic preserving schemes [31], both macroscopic flow variables and microscopic distribution function are updated. Hence, the collision term can be treated implicitly using the updated macroscopic flow variables. This has been applied on the construction of implicit UGKS for steady flows [1], where a prediction of the equilibrium state is carried out by solving the implicit macroscopic governing equations. This kind of implicit technique has been used in the study of radiative transfer [32] as well to remove the restriction of speed of light on the numerical time step.

The research in coupling of macroscopic and microscopic governing equations has been conducted by many others as well. In an earlier paper [33], a moment-based acceleration method has been developed by solving the coupled implicit system of the moment equations and kinetic equation iteratively. Such combination of the high-complexity physical model (high-order (HO) model) and the low-complexity ones (the low-order (LO) model) is named as the HOLO algorithm. A review

of the multiscale HOLO algorithms can be found in [34]. Similar idea has been used for fast convergence in many other kinetic methods [1,32], as well as in the Monte Carlo methods [35]. In order to develop an efficient implicit scheme for all flow regimes, especially to avoid the efficiency decrease in the continuum flows, a coupling of the HO kinetic equation and LO macroscopic equations and implicit treatment of collision term are necessary. More importantly, when the mesh size and time step are much larger than the particle mean free path and collision time, a multiscale flux function must be used in the update of macroscopic flow variables and microscopic distribution function. Otherwise, for the kinetic solvers with decoupled particle free transport and collision, the numerical dissipation would be proportional to the time step ( $\sim \Delta t$ ), which can become much larger than the physical one ( $\sim \tau$ ) in the continuum regime.

In order to fully utilize the multiscale nature of the UGKS, we propose an implicit UGKS (IUGKS) for unsteady flow simulations in all flow regimes. Starting from the direct modeling of conservation laws for conservative flow variables and the gas distribution function in a discretized space, a semi-discrete formulation is used to construct the implicit scheme. The residuals in the semi-discrete governing equations are evaluated from a time-averaged flux function over a local time step. This local time averaged flux function incorporates the cell size effect on the flow evolution. The multiscale transport property is maintained for an arbitrary large global time step. For unsteady flow simulation, implicit discretizations have been implemented for the evolution of macroscopic flow variables and gas distribution function. A matrix connecting the flow variables in the whole computational domain can be solved by the lower-upper symmetric Gauss-Seidel (LU-SGS) method [36,37], point-relaxation (PR) method [38], and the generalized minimal residual (GMRES) algorithm [39]. In the inner iterative process within each time-marching step, the implicit governing equations for macroscopic flow variables and microscopic distribution are solved alternatively to get convergent solution for the coupled macroscopic and microscopic systems. Many unsteady flow examples are used to validate the accuracy and efficiency of the IUGKS for the Euler, NS, as well as non-equilibrium simulation in the whole flow regimes.

This paper is organized as follows. Section 2 gives an introduction to the explicit UGKS and presents details in the construction of IUGKS. In Section 3, numerical validations and discussions are carried out. A conclusion is given in the last section.

## 2. Implicit unified gas-kinetic scheme

In this section, we will give a detailed description for both the explicit and implicit unified gas-kinetic schemes. For simplicity, the formulations are presented for two dimensional cases in this paper. Extension and implementation of the implicit algorithm in three dimensional space is straightforward.

### 2.1. Unified gas-kinetic scheme

The UGKS is a direct modeling method on the scales of time step and cell size. For a discrete finite volume cell  $i$  and discretized time step  $\Delta t = t^{n+1} - t^n$ , the governing equation for the gas distribution function is

$$f_i^{n+1} = f_i^n - \frac{1}{V_i} \sum_{j \in N(i)} \int_0^{\Delta t} u_n f_{ij}(t) S_{ij} dt + \int_0^{\Delta t} \Omega(f, f) dt, \quad (1)$$

where  $f_i$  is the cell averaged distribution function, and  $V_i$  is the volume of cell  $i$ .  $N(i)$  denotes the set of neighboring cells of  $i$ , and cell  $j$  is one of the neighbors. The interface connecting the cells  $i$  and  $j$  is referred to as  $ij$ . Hence,  $S_{ij}$  represents the area of the cell interface  $ij$ , and  $u_n = \mathbf{u} \cdot \mathbf{n}_{ij}$  is the normal component of the particles' microscopic velocity  $\mathbf{u}$ , where  $\mathbf{n}_{ij} = (\cos \theta, \sin \theta)^T$  is the normal vector of cell interface  $ij$  for two dimensional cases.  $f_{ij}(t)$  is a time-dependent distribution function, which describes the time evolution of flow physics around the cell interface  $ij$ . The collision term  $\Omega(f, f)$  takes into account the particles' interaction within one time step. Eq. (1) is an exact physical law for the discrete cell  $i$ , which simply describes the evolution of the gas distribution function due to particles' transport and collision on the discretized level. From the microscopic gas distribution function, the conservative variables can be obtained by taking moments

$$\mathbf{W} = \int f(u, v, \xi) \boldsymbol{\psi}(u, v, \xi) d\Xi, \quad (2)$$

where  $\boldsymbol{\psi}(u, v, \xi) = (1, u, v, \frac{1}{2}(u^2 + v^2 + \xi^2))^T$  and  $d\Xi = dudvd\xi$  for two dimensional cases.  $u$  and  $v$  are the particles' velocities along  $x$ - and  $y$ -directions, respectively.  $\xi$  denotes the particles' motion for  $K$  internal degrees of freedom, which has  $\xi^2 = \xi_1^2 + \dots + \xi_K^2$ .  $\mathbf{W}$  is a vector of conservative flow variables, i.e.,  $(\rho, \rho U, \rho V, \rho E)^T$  for the densities of mass, momentum and energy. By taking moments of Eq. (1), the corresponding macroscopic governing equations are

$$\mathbf{W}_i^{n+1} = \mathbf{W}_i^n - \frac{1}{V_i} \sum_{j \in N(i)} \int_0^{\Delta t} \int u_n f_{ij}(t) \boldsymbol{\psi}(u, v, \xi) S_{ij} dt d\Xi, \quad (3)$$

where the collision term is absent due to the compatibility condition

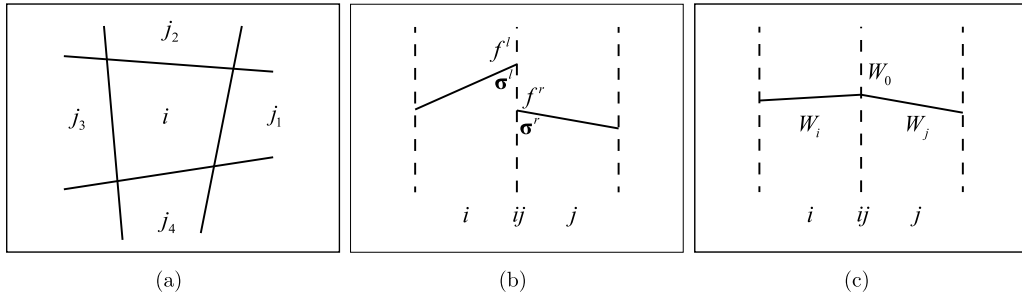


**Fig. 1.** Illustration for initial reconstruction in UGKS. (a) Stencil for spatial reconstruction; (b) initial reconstructed gas distribution function around a cell interface; (c) reconstructed conservative variables around a cell interface.

$$\int \Omega(f, f) \psi(u, v, \xi) d\Xi = \mathbf{0}. \tag{4}$$

Eq. (3) describes the conservations of mass, momentum and energy, which are exact as well.

As mentioned, the governing equations (1) and (3) are both the exact physical laws in a discretized space. The accuracy of the solutions from Eqs. (1) and (3) only depends on the modeling of the collision term and the flux transport, which is similar to the construction of constitutive relationship in the NS equations. The full Boltzmann collision term models the intermolecular interactions in a time scale less than the particle collision time. The numerical computation of the full Boltzmann collision term is too complicated which involves a five-fold integration. By using the fast spectral method [40–43], the computational cost of the collision term can be much reduced. However, for the UGKS the time step is not limited by the particle collision time  $\tau$ . In the comparative study [44], it is found that in the framework of the UGKS the full Boltzmann collision term and the kinetic model collision term give the same results when the time resolution  $\Delta t$  is larger than  $4\tau$ . For inhomogeneous numerical resolution with local  $\Delta t < 4\tau$ , the results from the kinetic model equation will deviate slightly from the Boltzmann solutions, such as temperature profile in shock structure. But, considering the computational simplicity and high efficiency these results are acceptable in engineering applications. Since the target in this paper is to develop an implicit scheme to accelerate the unsteady flow computation, a simple kinetic model equation is only considered, i.e.,  $\Omega(f, f) \approx (g - f)/\tau$ . An extension of the IUGKS with full Boltzmann collision term can be implemented by adopting a hybrid collision term of an explicit Boltzmann term and an implicit kinetic model term [44]. In the following, we will focus on the kinetic models.

The kinetic model equation with the relaxation collision term can be written as

$$\frac{\partial f}{\partial t} + \mathbf{u} \cdot \frac{\partial f}{\partial \mathbf{x}} = \frac{g - f}{\tau}, \tag{5}$$

where  $\tau$  is the particle mean collision time or the relaxation time. The equilibrium state  $g$  can be obtained from the macroscopic variables in the BGK model [45]

$$g = g_M = \rho \left( \frac{\lambda}{\pi} \right)^{\frac{k+2}{2}} e^{-\lambda((u-U)^2 + (v-V)^2 + \xi^2)} \tag{6}$$

for unit Prandtl number cases, or in the Shakhov model [46]

$$g = g_M \left[ 1 + (1 - Pr) \mathbf{c} \cdot \mathbf{q} \left( \frac{m_0 \mathbf{c}^2}{k_B T} - 5 \right) / \frac{5 p k_B T}{m_0} \right] \tag{7}$$

for monatomic gas cases with arbitrary Prandtl number  $Pr$ .  $\lambda$  is related to the temperature  $T$  by  $\lambda = m_0/2k_B T$ ,  $m_0$  is molecular mass, and  $k_B$  is the Boltzmann constant. In Eq. (7),  $g_M$  is the Maxwellian distribution given in Eq. (6),  $\mathbf{c}$  denotes the peculiar velocity.  $p = \rho/2\lambda$  is the pressure, and  $\mathbf{q}$  is the vector of heat fluxes, which is a third-order moment of the distribution function, i.e.,

$$\mathbf{q} = \frac{1}{2} \int (\mathbf{u} - \mathbf{U}) \left[ (u - U)^2 + (v - V)^2 + \xi^2 \right] f(u, v, \xi) d\Xi, \tag{8}$$

where  $\mathbf{U} = (U, V)^T$  is the macroscopic velocity.

For a second order accurate scheme, a linear initial distribution of flow variables inside a cell is required. For an arbitrary cell  $i$  as illustrated in Fig. 1(a), the initial distribution of the gas distribution function is constructed

$$f_i^n(\mathbf{x}) = f_i^n + \sigma_i(\mathbf{x} - \mathbf{x}_i), \tag{9}$$

from the cell averaged values in cell  $i$  and its neighbors. Here,  $\sigma_i$  is the spatial derivative of the gas distribution function and  $\mathbf{x}_i$  denotes the center of cell  $i$ .

The multi-scale nature of the UGKS comes from the construction of a time-dependent distribution function at the cell interface,  $f_{ij}(t)$ , which takes collision effect into the particle transport. In the evolution process of UGKS, the fluxes across cell interface are constructed from the analytic solution of the BGK equation (5), i.e.,

$$f(\mathbf{x}_0, t, u, v, \xi) = \frac{1}{\tau} \int_0^t g(\mathbf{x}', t', u, v, \xi) e^{-(t-t')/\tau} dt' + e^{-t/\tau} f_0(\mathbf{x}_0 - \mathbf{u}t, u, v, \xi) \tag{10}$$

where  $\mathbf{x}_0$  denotes the center of cell interface. In order to construct the time-dependent distribution function in Eq. (10), the initial gas distribution function  $f_0(\mathbf{x}, u, v, \xi)$  and the equilibrium state  $g(\mathbf{x}, t, u, v, \xi)$  around the cell interface should be provided first. For the cell interface  $ij$ , without loss of generality it is assumed  $\mathbf{x}_0 = \mathbf{0}$ . With the reconstructed piecewise distribution function in Eq. (9), the initial state of the gas distribution function around the interface is

$$f_0(\mathbf{x}) = \begin{cases} f^l + \boldsymbol{\sigma}^l \cdot \mathbf{x}, & \mathbf{x} \cdot \mathbf{n}_{ij} \leq 0, \\ f^r + \boldsymbol{\sigma}^r \cdot \mathbf{x}, & \mathbf{x} \cdot \mathbf{n}_{ij} > 0, \end{cases} \tag{11}$$

where  $f^l$  and  $f^r$  are the distribution functions on the left and right sides of the interface, and  $\boldsymbol{\sigma}^l$  and  $\boldsymbol{\sigma}^r$  are the corresponding spatial derivatives. Specifically, as shown in Fig. 1(b),  $f^l = f_i^n(\mathbf{x}_0)$ ,  $f^r = f_j^n(\mathbf{x}_0)$ ,  $\boldsymbol{\sigma}^l = \boldsymbol{\sigma}_i$  and  $\boldsymbol{\sigma}^r = \boldsymbol{\sigma}_j$ . For the equilibrium state, the Taylor expansion in time and space gives

$$g(\mathbf{x}, t) = g_0 + g_x \cdot \mathbf{x} + g_t t, \tag{12}$$

where  $g_0$  is the initial equilibrium state on the interface obtained by Eq. (6) or (7), in which the required macroscopic variables comes from the moments of the initial gas distribution function  $f^l$  and  $f^r$ . As shown in Fig. 1(c), we have

$$\mathbf{W}_0 = \int_{u_n > 0} f^l \boldsymbol{\psi} d\Xi + \int_{u_n < 0} f^r \boldsymbol{\psi} d\Xi. \tag{13}$$

Together with the cell averaged macroscopic variables around the interface, the spatial derivatives can be obtained

$$\mathbf{W}_x = \mathbf{W}_x^l (1 - H[x_n]) + \mathbf{W}_x^r H[x_n], \tag{14}$$

where  $H[x]$  is the Heaviside function defined by

$$H[x] = \begin{cases} 0, & x < 0; \\ 1, & x \geq 0. \end{cases} \tag{15}$$

Fig. 1(c) shows the distribution of the macroscopic variables near the interface, where  $\mathbf{W}$  is continuous and has two slopes, i.e.,  $\mathbf{W}_x^l$  and  $\mathbf{W}_x^r$ . Then from the compatibility condition (4) the temporal derivative at the initial instant can be computed by a Lax-Wendroff method

$$\mathbf{W}_t = \frac{\partial}{\partial t} \int g(t) \boldsymbol{\psi} d\Xi = \frac{\partial}{\partial t} \int f(t) \boldsymbol{\psi} d\Xi = - \int \mathbf{u} \cdot [\boldsymbol{\sigma}^l H[u_n] + \boldsymbol{\sigma}^r (1 - H[u_n])] \boldsymbol{\psi} d\Xi. \tag{16}$$

Since the Maxwellian distribution has one-to-one correspondence with the flow conservative variables, the spatial derivative  $g_x$  and temporal derivative  $g_t$  of the equilibrium state can be easily obtained from  $\mathbf{W}_x$  and  $\mathbf{W}_t$ . At this point, the time-dependent distribution function at the cell interface has been constructed

$$\begin{aligned} f_{ij}(t) &= (1 - e^{-t/\tau})g_0 + e^{-t/\tau} f^{l,r} \\ &+ \tau(e^{-t/\tau} - 1 + \frac{t}{\tau}e^{-t/\tau})(\mathbf{u} \cdot \mathbf{g}_x^{l,r}) + \tau(\frac{t}{\tau} + e^{-t/\tau} - 1)g_t \\ &- \tau(\frac{t}{\tau}e^{-t/\tau})(\mathbf{u} \cdot \boldsymbol{\sigma}^{l,r}), \end{aligned} \tag{17}$$

where the superscript  $l$  and  $r$  denote the left and right states according to the Heaviside function  $H[u_n]$ .

With Eq. (17), the multiscale fluxes for microscopic and macroscopic variables can be computed. Then the conservative variables can be updated first by Eq. (3), and the collision term in Eq. (1) can be discretized in an implicit way by the trapezoidal rule

$$\int_0^{\Delta t} \Omega(f, f) = \frac{\Delta t}{2} \left( \frac{g_i^{n+1} - f_i^{n+1}}{\tau_i^{n+1}} + \frac{g_i^n - f_i^n}{\tau_i^n} \right), \tag{18}$$

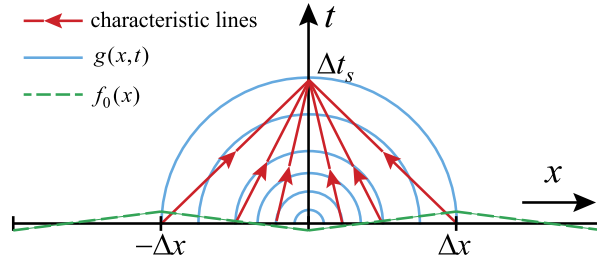


Fig. 2. Physical picture illustrating the time evolution of flow physics around a cell interface in GKS and UGKS.

where  $g^{n+1}$  is computed by the newly updated macroscopic variables. Subsequently, the distribution function can be updated by Eq. (1).

The above UGKS is a truly multiscale method, which adopts a scale-adaptive flux function coupling the particles' free transport and collision. From the analytic solution in Eqs. (10) and (17), we can observe a transition from the initial non-equilibrium distribution function to the equilibrium one with an increment of time. This process models a transition from kinetic scale to hydrodynamic scale physics. It describes an accumulating effect from particle collision in the evolution process. The physical picture is illustrated in Fig. 2, where a time evolution of flow physics around the interface within a cell-size-determined time step  $\Delta t_s$  is presented. The automatic scale transition in the physical solution depends on the ratio of  $t/\tau$ , which is the key ingredient to construct a multiscale method. More details about the implementation of the explicit UGKS can be found in [8] and [10].

For the explicit UGKS, the basic assumptions are a local constant  $\tau$  and the local distributed flow variables in the form of Eq. (11) and Eq. (12). Therefore, the analytic solution (17) is valid in a local region in space and time with a cell size  $\Delta x$  and a time step  $\Delta t_s$ , which are connected by the local CFL condition, see Fig. 2. Eq. (1), Eq. (3) and Eq. (17) are fundamental physical laws, which present a local flow evolution in an explicit way. As equations-based formulation Eq. (1) and Eq. (3) can be transformed into semi-discrete forms for the construction of an implicit scheme, the acceleration techniques in CFD can be easily employed here in the UGKS.

### 2.2. Time-accurate implicit UGKS

From Eq. (1) and Eq. (3), the semi-discrete macroscopic governing equations for conservative variables can be written as

$$\frac{\partial \mathbf{W}_i}{\partial t} + \frac{1}{V_i} \sum_{j \in N(i)} \hat{\mathbf{F}}_{ij} S_{ij} = \mathbf{0}, \tag{19}$$

where  $\hat{\mathbf{F}}_{ij}$  is the macroscopic flux across the cell interface. The governing equation for the gas distribution function is

$$\frac{\partial f_i}{\partial t} + \frac{1}{V_i} \sum_{j \in N(i)} u_n \hat{f}_{ij} S_{ij} = \frac{g_i - f_i}{\tau_i}, \tag{20}$$

where  $u_n \hat{f}_{ij}$  is the interface flux of the gas distribution function. The above semi-discrete formulations describe the instantaneous variation of the flow field. It seems to present the flow evolution in a time scale  $t \rightarrow 0$ . Although Eq. (19) and Eq. (20) are still consistent with the UGKS formulation, it reduces the time-dependent UGKS fluxes into a particle free transport, which makes UGKS as a standard single scale DVM method. Therefore, in order to incorporate the multiscale property of UGKS into the above formulation, it is better to reconstruct the interface fluxes in Eq. (19) and Eq. (20) as a time-averaged flux instead of instantaneous one. Specifically, the above fluxes are averaged over a cell-size-determined time step, which is shown in Fig. 2. Therefore, a cell-size-dependent flow evolution is implicitly included in the semi-discrete governing equations. In order to distinguish the cell-size-determined time step from the numerical marching time step  $\Delta t$  for an implicit scheme, this time step is given by  $\Delta t_s$  which determines the local flow physics.  $\Delta t_s$  is the same as the explicit local time step, which is computed by the local CFL number less than one. The semi-discrete Eq. (19) and Eq. (20) have multiscale nature.

For a large numerical marching time step  $\Delta t = t^{n+1} - t^n$ , we have the discrete macroscopic governing equations

$$\frac{\mathbf{W}_i^{n+1} - \mathbf{W}_i^n}{\Delta t} + \frac{1}{V_i} \sum_{j \in N(i)} (\epsilon \hat{\mathbf{F}}_{ij}^{n+1} + (1 - \epsilon) \hat{\mathbf{F}}_{ij}^n) S_{ij} = \mathbf{0}, \tag{21}$$

and the discrete microscopic equations

$$\frac{f_i^{n+1} - f_i^n}{\Delta t} + \frac{1}{V_i} \sum_{j \in N(i)} u_n (\epsilon \hat{f}_{ij}^{n+1} + (1 - \epsilon) \hat{f}_{ij}^n) S_{ij} = \epsilon \frac{g_i^{n+1} - f_i^{n+1}}{\tau_i^{n+1}} + (1 - \epsilon) \frac{g_i^n - f_i^n}{\tau_i^n}, \tag{22}$$

where  $\hat{\mathbf{F}}_{ij}^{n+1}$  and  $\hat{\mathbf{F}}_{ij}^n$  denote the macroscopic fluxes computed by taking moments of the microscopic flux of a gas distribution function. Here  $u_n \hat{f}_{ij}^{n+1}$  and  $u_n \hat{f}_{ij}^n$  are the time-averaged fluxes over  $\Delta t_s$  from the explicit UGKS formulation. For  $\epsilon = 0.5$  in Eq. (21) and Eq. (22), it corresponds to the Crank-Nicolson method with second-order accuracy in time, and for  $\epsilon = 1$  it is a backward Euler scheme with first-order temporal accuracy.

Eq. (21) and Eq. (22) are fully coupled and  $g_i^{n+1}$  in Eq. (22) has one-to-one correspondence with  $\mathbf{W}_i^{n+1}$  in Eq. (21). It is difficult to simultaneously solve these two implicit systems. Instead we can solve Eq. (21) and Eq. (22) in an alternative way. Specifically, we first get an approximate equilibrium state  $\tilde{g}^{n+1}$  from Eq. (21) from an assumed approximate solution  $f^{n+1}$ , then obtain a more precise solution of  $f^{n+1}$  from Eq. (22) using the previously obtained  $\tilde{g}^{n+1}$ . After several iterations, both  $f^{n+1}$  and  $g^{n+1}$  can be updated. This process isn't equivalent to getting solutions from Eq. (21) and Eq. (22) directly, because the implicit multiscale fluxes have to be evaluated as well on the left hand sides of these equations. These equations will result in a large nonlinear system, especially for a second-order accurate numerical fluxes. Therefore, implicit schemes usually adopt a delta-form equation with implicit parts on left hand side and explicit parts on right hand side of an equation [25]. Based on the delta-form equations, the implicit parts on the left hand side can be much simplified using a first-order flux function, and it becomes much easier to take iterative processes to solve the implicit system [26]. Details are given in the following.

Given an intermediate approximate solution  $\mathbf{W}^{(s)}$  and  $f^{(s)}$ , the delta-form governing equations of Eq. (21) and Eq. (22) for iterative algorithm can be written as

$$\frac{1}{\Delta t} \Delta \mathbf{W}_i^{(s)} + \frac{\epsilon}{V_i} \sum_{j \in N(i)} \Delta \hat{\mathbf{F}}_{ij}^{(s)} S_{ij} = \mathbf{R}_i^{(s)}, \tag{23}$$

and

$$\left( \frac{\epsilon}{\tau_i^{(s+1)}} + \frac{1}{\Delta t} \right) \Delta f_i^{(s)} + \frac{\epsilon}{V_i} \sum_{j \in N(i)} u_n S_{ij} \Delta \hat{f}_{ij}^{(s)} = r_i^{(s)}, \tag{24}$$

where

$$\mathbf{R}_i^{(s)} = \frac{\mathbf{W}_i^n - \mathbf{W}_i^{(s)}}{\Delta t} - \frac{1}{V_i} \sum_{j \in N(i)} \left( (1 - \epsilon) \hat{\mathbf{F}}_{ij}^n + \epsilon \hat{\mathbf{F}}_{ij}^{(s)} \right) S_{ij}, \tag{25}$$

and

$$r_i^{(s)} = \frac{f_i^n - f_i^{(s)}}{\Delta t} - \frac{1}{V_i} \sum_{j \in N(i)} u_n \left( \epsilon \hat{f}_{ij}^{(s)} + (1 - \epsilon) \hat{f}_{ij}^n \right) S_{ij} + \epsilon \frac{\tilde{g}_i^{(s+1)} - f_i^{(s)}}{\tau_i^{(s+1)}} + (1 - \epsilon) \frac{g_i^n - f_i^n}{\tau_i^n}, \tag{26}$$

with  $\Delta \mathbf{W}_i^{(s)} = \tilde{\mathbf{W}}_i^{(s+1)} - \mathbf{W}_i^{(s)}$  and  $\Delta f_i^{(s)} = f_i^{(s+1)} - f_i^{(s)}$ . The fluxes in  $r_i^{(s)}$  and  $\mathbf{R}_i^{(s)}$  are fully evaluated by the UGKS over a time step  $\Delta t_s$ , i.e.,

$$\hat{\mathbf{F}}_{ij} = \frac{1}{\Delta t_s} \int_0^{\Delta t_s} \int u_n f_{ij}(t) \boldsymbol{\psi}(u, v, \xi) dt d\Xi, \tag{27}$$

and

$$u_n \hat{f}_{ij} = \frac{1}{\Delta t_s} \int_0^{\Delta t_s} u_n f_{ij}(t) dt, \tag{28}$$

where  $f_{ij}(t)$  is given in Eq. (17).

For the terms on the left hand side of Eq. (23), the Euler equations-based fluxes

$$\Delta \hat{\mathbf{F}}_{ij}^{(s)} = \frac{1}{2} \left[ \Delta \mathbf{T}_i^{(s)} + \Delta \mathbf{T}_j^{(s)} + \Gamma_{ij} \left( \Delta \mathbf{W}_i^{(s)} - \Delta \mathbf{W}_j^{(s)} \right) \right] \tag{29}$$

are adopted to simplify the implicit macroscopic fluxes, where  $\mathbf{T}$  are the Euler fluxes

$$\begin{aligned} \mathbf{T} &= \mathbf{T}_x \cos \theta + \mathbf{T}_y \sin \theta, \\ \mathbf{T}_x &= \left[ \rho U, \rho U^2 + p, \rho UV, U(\rho E + p) \right]^T, \\ \mathbf{T}_y &= \left[ \rho V, \rho UV, \rho V^2 + p, V(\rho E + p) \right]^T, \end{aligned} \tag{30}$$

and  $\Gamma_{ij}$  is the spectral radius of the Euler flux Jacobian with an additional kinematic viscosity related stable factor [47], i.e.,

$$\Gamma_{ij} = |\mathbf{U}_{ij} \cdot \mathbf{n}_{ij}| + a_s + \frac{2\mu}{\rho|\mathbf{n}_{ij} \cdot (\mathbf{x}_j - \mathbf{x}_i)|}, \tag{31}$$

where  $\mathbf{U}_{ij}$  is macroscopic velocity and  $a_s$  is the speed of sound. For simplifying the numerical fluxes on the left hand side of Eq. (24), we use an upwind approach

$$\Delta \hat{f}_{ij}^{(s)} = \frac{1}{2} [1 + \text{sign}(u_n)] \Delta f_i^{(s)} + \frac{1}{2} [1 - \text{sign}(u_n)] \Delta f_j^{(s)}. \tag{32}$$

Substituting Eq. (27) and Eq. (28) into Eq. (23) and Eq. (24), the implicit governing equations for conservative flow variables become

$$C_i \Delta \mathbf{W}_i^{(s)} + \frac{1}{2V_i} \sum_{j \in N(i)} \epsilon_{ij} S_{ij} \left[ T(\mathbf{W}_j^{(s)} + \Delta \mathbf{W}_j^{(s)}) - T(\mathbf{W}_j^{(s)}) - \Gamma_{ij} \Delta \mathbf{W}_j^{(s)} \right] = \mathbf{R}_i^{(s)}, \tag{33}$$

where

$$C_i = \frac{1}{\Delta t} + \frac{1}{2V_i} \sum_{j \in N(i)} \epsilon_{ij} \Gamma_{ij} S_{ij}. \tag{34}$$

The implicit governing equation for gas distribution function is

$$D_i \Delta f_i^{(s)} + \sum_{j \in N(i)} D_j \Delta f_j^{(s)} = r_i^{(s)}, \tag{35}$$

where

$$D_i = \frac{\epsilon}{\tau_i^{(s+1)}} + \frac{1}{\Delta t} + \frac{1}{2V_i} \sum_{j \in N(i)} u_n \epsilon_{ij} S_{ij} [1 + \text{sign}(u_n)],$$

$$D_j = \frac{1}{2V_i} u_n \epsilon_{ij} S_{ij} [1 - \text{sign}(u_n)]. \tag{36}$$

For the above delta-form implicit equations, the LU-SGS method [36,37], the point-relaxation (PR) method [38], or the GMRES algorithm [39] can be applied to solve the variation of conservative variables and the gas distribution function. In the current paper, we employ the PR(2) scheme described in [38], in which each inner iterative process is dealt with twice forward and backward sweeps. The details for solving the matrix system will not be further discussed, see [1,38]. Therefore, starting with  $\mathbf{W}^{(s=0)} = \mathbf{W}^n$  and  $f^{(s=0)} = f^n$ , Eq. (33) and Eq. (35) can be alternatively solved within several inner iterations.

In summary, the time evolution of the implicit UGKS for unsteady flow simulations from  $t^n$  to  $t^{n+1}$  can be described as

- Step 1** Calculate the time interval  $\Delta t_s$ -averaged numerical fluxes  $\hat{\mathbf{F}}_{ij}^n$  and  $u_n \hat{f}_{ij}^n$  using the gas distribution function  $f^n$  and equilibrium state  $g^n$  by the explicit UGKS fluxes.
- Step 2** Compute the time interval  $\Delta t_s$ -averaged intermediate fluxes  $\mathbf{F}_{ij}^{(s)}$  and  $u_n \hat{f}_{ij}^{(s)}$  using the intermediate solution  $f^{(s)}$  and  $\mathbf{W}^{(s)}$  by Eq. (27) and Eq. (28). For the first inner step,  $f^{(s=0)} = f^n$  and  $g^{(s=0)} = g^n$  are adopted.
- Step 3** Evaluate the macroscopic residual  $\mathbf{R}_i^{(s)}$  in Eq. (25) using the numerical macroscopic fluxes obtained in Step 1 and Step 2.
- Step 4** Solve Eq. (33) to obtain  $\Delta \mathbf{W}^{(s)}$ , then get the equilibrium state  $\tilde{g}_i^{(s+1)}$  from  $\tilde{\mathbf{W}}^{(s+1)} = \mathbf{W}^{(s)} + \Delta \mathbf{W}^{(s)}$  by Eq. (6) or Eq. (7).
- Step 5** Evaluate the microscopic residual  $r^{(s)}$  in Eq. (26) using the equilibrium state  $\tilde{g}_i^{(s+1)}$  obtained in Step 4 and the micro-fluxes  $u_n \hat{f}_{ij}^n$  and  $u_n \hat{f}_{ij}^{(s)}$  evaluated in Step 1 and Step 2.
- Step 6** Solve Eq. (35) to obtain  $\Delta f^{(s)}$ , then get the gas distribution function from  $f_i^{(s+1)} = f_i^{(s)} + \Delta f_i^{(s)}$ , and the conservative variables  $\mathbf{W}_i^{(s+1)}$  by taking moments of  $f_i^{(s+1)}$  in Eq. (2).
- Step 7** Check the convergence through  $L_2$  norm of the macroscopic residual  $\mathbf{R}^{(s)}$  (if necessary, e.g. in homogeneous cases, check  $r^{(s)}$  instead to measure the convergence of gas distribution function.)
  - if the residual is small enough, update the solutions  $f^{n+1}$  and  $\mathbf{W}^{n+1}$  by the newly obtained  $f^{(s+1)}$  and  $\mathbf{W}^{(s+1)}$ , and stop the inner iterations.
  - if not, go to Step 2 and continue the inner iterations.

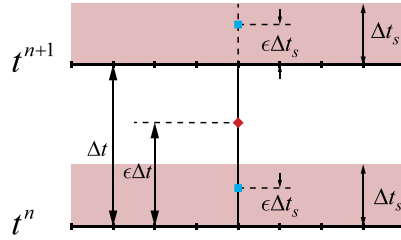


Fig. 3. Structure of temporal discretization.

### 2.3. Modification for temporal discretization

The time-averaged fluxes are evaluated over a finite time step  $\Delta t_s$  instead of at the instant of  $t^{n+1}$  and  $t^n$ . When the evolution time step  $\Delta t$  is comparable with  $\Delta t_s$ , the size of  $\Delta t_s$  should not be ignored in the temporal discretization. As illustrated in Fig. 3, the fluxes at time  $t^n + \epsilon \Delta t$  can be approximated by those at time  $t^n + \epsilon \Delta t_s$  and  $t^{n+1} + \epsilon \Delta t_s$  with weighted coefficients

$$\begin{aligned} \epsilon' &= \frac{\epsilon \Delta t - \epsilon \Delta t_s}{\Delta t}, \\ 1 - \epsilon' &= \frac{(1 - \epsilon) \Delta t + \epsilon \Delta t_s}{\Delta t}. \end{aligned} \tag{37}$$

Then Eq. (21) and Eq. (22) become

$$\frac{\mathbf{W}_i^{n+1} - \mathbf{W}_i^n}{\Delta t} + \frac{1}{V_i} \sum_{j \in N(i)} \left( \epsilon' \hat{\mathbf{F}}_{ij}^{n+1} + (1 - \epsilon') \hat{\mathbf{F}}_{ij}^n \right) S_{ij} = \mathbf{0}, \tag{38}$$

and

$$\frac{f_i^{n+1} - f_i^n}{\Delta t} + \frac{1}{V_i} \sum_{j \in N(i)} u_n \left( \epsilon' \hat{f}_{ij}^{n+1} + (1 - \epsilon') \hat{f}_{ij}^n \right) S_{ij} = \epsilon \frac{g_i^{n+1} - f_i^{n+1}}{\tau_i^{n+1}} + (1 - \epsilon) \frac{g_i^n - f_i^n}{\tau_i^n}, \tag{39}$$

where the modification is only applied to the flux evaluation terms. The delta-form of governing equations can be written as

$$\frac{1}{\Delta t} \Delta \mathbf{W}_i^{(s)} + \frac{\epsilon'}{V_i} \sum_{j \in N(i)} \Delta \hat{\mathbf{F}}_{ij}^{(s)} S_{ij} = \mathbf{R}_i^{(s)}, \tag{40}$$

and

$$\left( \frac{\epsilon}{\tau_i^{(s+1)}} + \frac{1}{\Delta t} \right) \Delta f_i^{(s)} + \frac{\epsilon'}{V_i} \sum_{j \in N(i)} u_n S_{ij} \Delta \hat{f}_{ij}^{(s)} = r_i^{(s)}, \tag{41}$$

where

$$\mathbf{R}_i^{(s)} = \frac{\mathbf{W}_i^n - \mathbf{W}_i^{(s)}}{\Delta t} - \frac{1}{V_i} \sum_{j \in N(i)} \left( (1 - \epsilon') \hat{\mathbf{F}}_{ij}^n + \epsilon' \hat{\mathbf{F}}_{ij}^{(s)} \right) S_{ij},$$

and

$$r_i^{(s)} = \frac{f_i^n - f_i^{(s)}}{\Delta t} - \frac{1}{V_i} \sum_{j \in N(i)} u_n \left( \epsilon' \hat{f}_{ij}^{(s)} + (1 - \epsilon') \hat{f}_{ij}^n \right) S_{ij} + \epsilon \frac{g_i^{(s+1)} - f_i^{(s)}}{\tau_i^{(s+1)}} + (1 - \epsilon) \frac{g_i^n - f_i^n}{\tau_i^n}.$$

Particularly, when  $\Delta t = \Delta t_s$ ,  $\epsilon'$  equals zero. The governing equations automatically reduce to the explicit UGKS where both macroscopic variables and distribution function are updated within one inner iteration only. For the C-N scheme with  $\epsilon = 1/2$ , the collision term is approximated by trapezoidal rules. It should be noted that without the modified coefficient  $\epsilon'$  the early implicit UGKS cannot directly go to the explicit scheme. Even though it can still get identical solutions, it may take several inner iterations to obtain the convergent solutions.

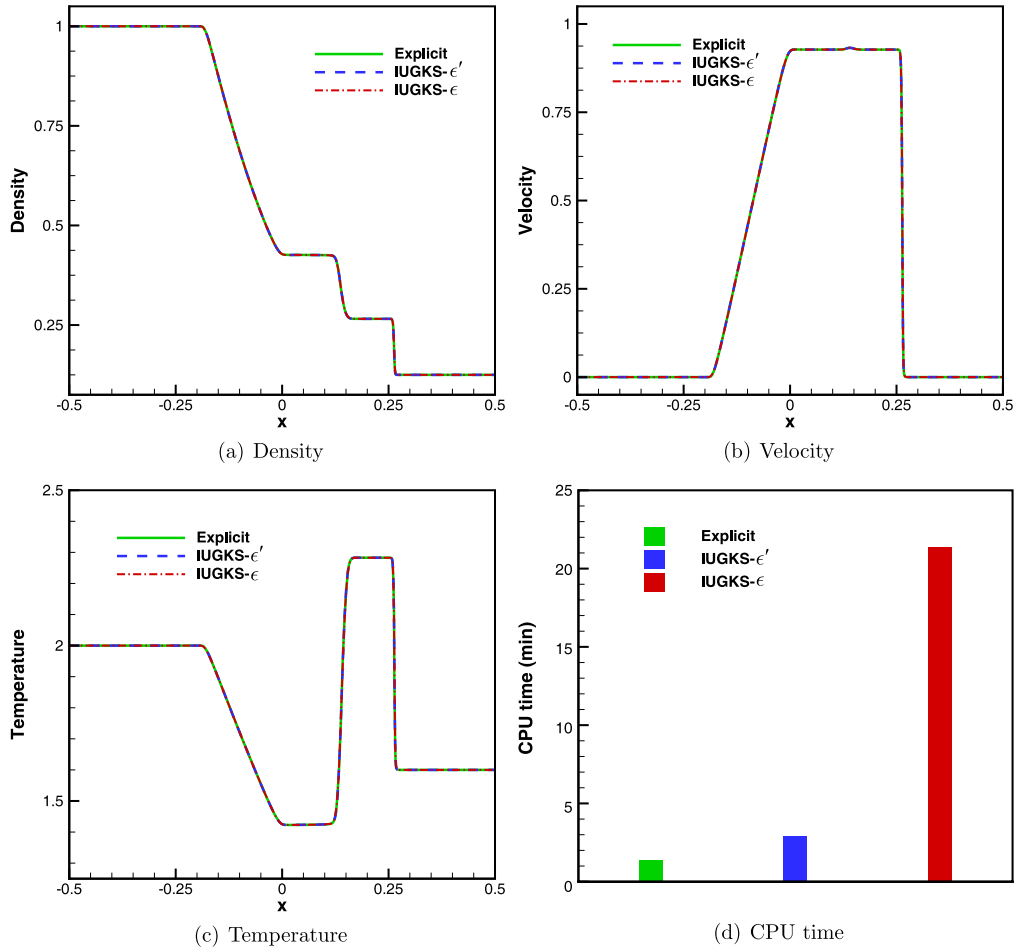


**Fig. 4.** Numerical results and computational cost of the Sod's shock tube problems at  $Kn = 1.0 \times 10^{-4}$  obtained from the explicit UGKS, IUGKS- $\epsilon$  and IUGKS- $\epsilon'$  with  $\Delta t = \Delta t_s$ .  $\epsilon = 0.5$  is adopted for the implicit schemes and it corresponds to  $\epsilon' = 0$  for IUGKS- $\epsilon'$ .

### 3. Numerical validation

#### 3.1. Sod's shock tube

Sod's shock tube is computed to validate the IUGKS for unsteady flows in one-dimensional case. The initial condition is given by

$$\begin{aligned}
 (\rho_l, \rho_l U_l, p_l) &= (1.0, 0.0, 1.0), & x \leq 0; \\
 (\rho_r, \rho_r U_r, p_r) &= (0.125, 0.0, 0.1), & x > 0.
 \end{aligned}$$

The time steps are denoted by CFL numbers,

$$\Delta t = \text{CFL} \frac{\Delta x}{\max |u_k|}. \tag{42}$$

For the explicit UGKS, CFL = 0.5 is adopted, which is also used to give the scale-dependent time step  $\Delta t_s$  for evaluating the time-averaged fluxes in the implicit scheme.

First of all, we compute the Sod's shock tube problem at  $Kn = 10^{-4}$  with a small time step of  $\Delta t = \Delta t_s$ . The computational domain is discretized into 1000 uniform cells. Comparison between the implicit schemes with the original  $\epsilon$  and the modified  $\epsilon'$  is carried out when the time step becomes as small as that used in the explicit scheme. For simplification, in the following the IUGKS with  $\epsilon$  will be denoted by IUGKS- $\epsilon$ , and the other one with  $\epsilon'$  will be IUGKS- $\epsilon'$ . In this case,  $\epsilon = 0.5$  for the C-N method is chosen to give a second-order accuracy in time, and  $\epsilon'$  will become 0 due to  $\Delta t = \Delta t_s$ . Distributions of density, velocity and temperature at the time  $t = 0.15$  are given in Fig. 4. It can be observed that both implicit schemes can give identical solutions to that of explicit UGKS. The computational cost is shown in Fig. 4(d), where IUGKS- $\epsilon'$  is comparable with the explicit scheme and is much cheaper than IUGKS- $\epsilon$ . The reason has been given in Section 2.3 that

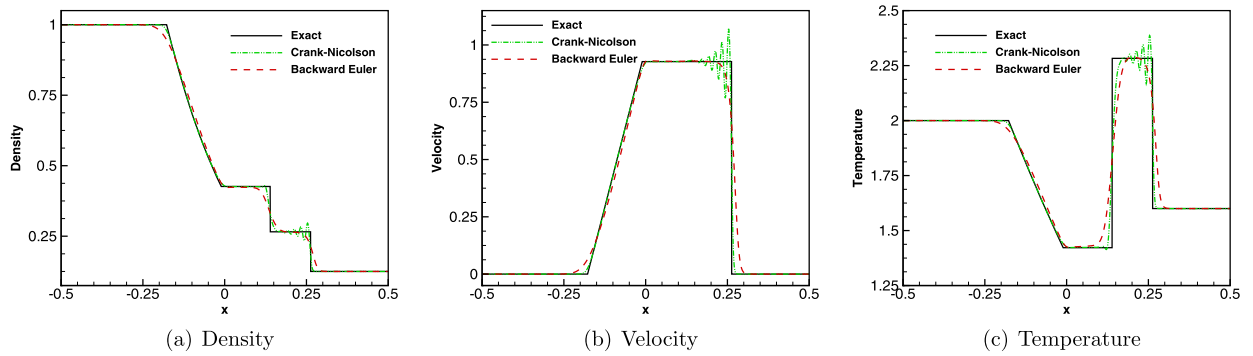


**Fig. 5.** Comparison of two different temporal discretization methods, i.e., the Crank-Nicolson method and the backward Euler scheme for IUGKS- $\epsilon'$  in the Sod test case with CFL = 50.

IUGKS- $\epsilon'$  with  $\Delta t = \Delta t_s$  automatically reduces to the explicit scheme and only one inner iteration is needed for each time step. However, for IUGKS- $\epsilon$  several inner iterations are still needed to get a convergent solution in each time step.

Different values of  $\epsilon$  correspond to different temporal discretization methods. Two typical discretization methods for the IUGKS- $\epsilon'$  are presented in the Sod's test with CFL = 50. Distributions of density, velocity and temperature obtained from IUGKS- $\epsilon'$  with  $\epsilon = 0.5$  of the C-N scheme, and  $\epsilon = 1$  of the backward Euler method are given in Fig. 5. As observed in the papers [27,48], due to the dispersion characteristics of the C-N scheme, numerical oscillations will appear around the normal shock wave in the large time step evolution. Regardless of numerical oscillations, the C-N scheme can give a sharp discontinuity, while the backward Euler scheme can effectively suppress the numerical oscillations around the smeared normal shock wave. Therefore, for a balance of capturing discontinuity and accuracy preserving, a selection of proper  $\epsilon$  in the interval of [0.5, 1] is necessary. Based on this case, we give the velocity distribution around the shock discontinuity for different  $\epsilon$  in Fig. 6(a). It can be observed that among these cases the one with  $\epsilon = 0.7$  gives the best result, which has no obvious oscillation and shows less dissipation. A group of test results for the cases with different  $\epsilon$  and time steps are illustrated in Fig. 6(b). For C-N scheme, it will give oscillation near the shock discontinuities unless the time step is not too large. With the increment of  $\epsilon$ , the dispersion error will gradually be reduced and the time step used could be increased. When  $\epsilon$  goes up to a specific value, the numerical scheme becomes stable enough. The dashed line in Fig. 6(b) may help to give a rough impression of how to choose the parameter  $\epsilon$ . The basic principles are the followings: (a) using a relatively large value of  $\epsilon$  to maintain the numerical stability for discontinuities; (b) using as small value of  $\epsilon$  as possible to achieve higher accuracy. In practice, a general suggestion is that for continuum flows with un-resolved discontinuities, a moderate  $\epsilon$ , such as 0.75, and a large time step can be used first to obtain a tentative solution. Under such a condition the numerical scheme is efficient and stable, and the numerical result is supposed to be more accurate than that obtained from backward Euler scheme with  $\epsilon = 1$ . If a more accurate solution is required, we can choose a smaller time step and slightly reduce the parameter  $\epsilon$  until a satisfactory result has been obtained. It should be noted that only for the cases in the continuum flow regime with un-resolved shock discontinuity, the selection of  $\epsilon$  is required. For rarefied smooth flows or well-resolved shock waves,  $\epsilon = 0.5$  can be directly applied for second order accurate solutions. From our test cases in the current paper, it seems that the results will not be sensitive to the selection of  $\epsilon$ . Therefore, except for the accuracy testing cases,  $\epsilon = 0.75$  is preferred in the current paper with a balance between accuracy and efficiency.

In order to figure out the efficiency acceleration of the implicit scheme, we compute the Sod case using IUGKS- $\epsilon'$  with  $\epsilon = 0.75$  and different time steps. The computational domain is discretized into 400 nonuniform cells with a minimum cell size of  $2 \times 10^{-4}$  and a maximum cell size of 0.01. The results in both continuum and rarefied flow regimes are given in Fig. 7, which are compared with the solutions from the explicit UGKS. For the continuum case at  $Kn = 10^{-4}$ , the velocity space is discretized into 200 velocity points, where the trapezoidal rule is used for the moments integration. The computational costs are listed in Table 1. It can be seen that generally the IUGKS- $\epsilon'$  is more than ten times faster than the explicit UGKS in the continuum regime. For the rarefied flow at  $Kn = 10$ , we employ a non-uniform mesh with 200 cells which has a smallest cell size of 0.0005 around the initial discontinuity. In order to get rid of the ray effect and to obtain a smooth solution, we employ 20000 points for velocity space discretization. Actually, using uniform mesh and much fewer velocity points can also give acceptable results for this case, but here we use the much large number of grid points for testing the efficiency of the schemes. The computational cost and acceleration rate from IUGKS are listed in Table 2 for the rarefied case. It can be observed that for a reasonably good result, e.g. the one with CFL = 50, the computational efficiency can increase by dozens of times.

### 3.2. Couette flow with a temperature gradient

In the incompressible limit, the Couette flow with a temperature gradient has a steady state analytic solution under the assumption of constant viscosity and heat conduction coefficients. Such a steady state problem provides a good test case to validate the spatial accuracy of the IUGKS. This case describes the flow between two parallel solid boundaries. The setup is

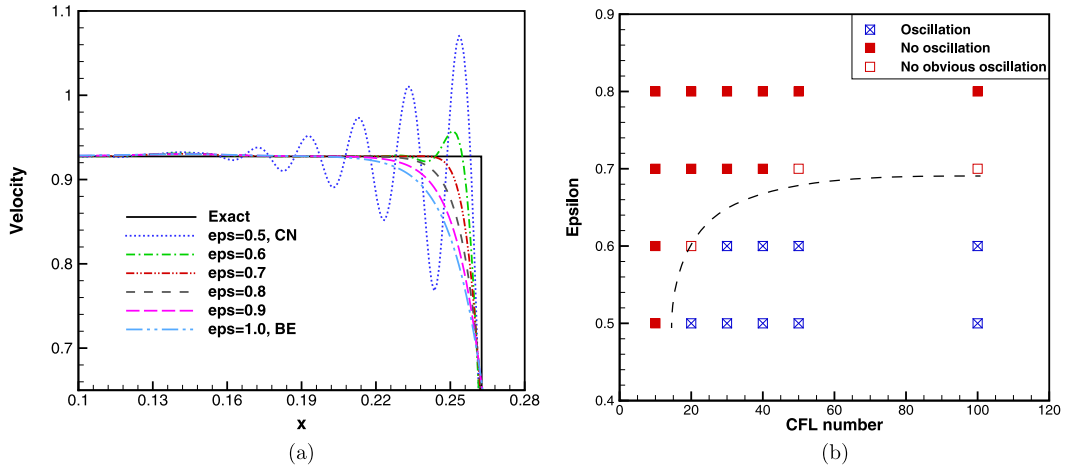


**Fig. 6.** Assessment of the influence of  $\epsilon$  on the numerical results around the shock discontinuity. (a) Velocity distribution around the shock discontinuity for cases with different  $\epsilon$ ; (b) results obtained from the IUGKS with different  $\epsilon$  using different time steps.

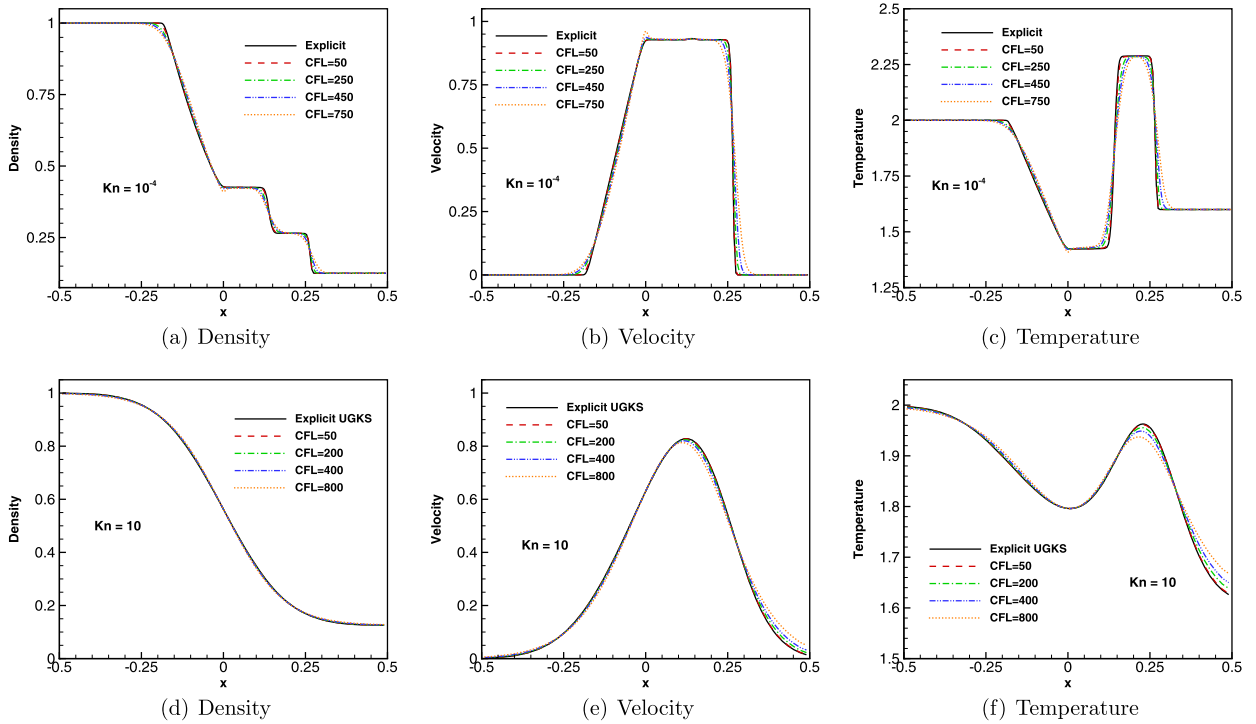


**Fig. 7.** Numerical results of the Sod test case from IUGKS- $\epsilon'$  with different choices of time step. The upper ones are the results at  $Kn = 10^{-4}$ , and the lower ones are those at  $Kn = 10$ .

**Table 1**

Computational cost of the implicit UGKS and the explicit UGKS for the Sod test case at  $Kn = 10^{-4}$  with different time steps.

	Explicit UGKS	IUGKS- $\epsilon'$ with $\epsilon = 0.75$			
CFL number	0.5	50	250	450	750
CPU time (sec)	159.6	23.9	9.2	6.6	5.6
Speedup	1.0	6.7	17.4	24.3	28.7

as follows. The top solid boundary has a constant temperature  $T_1$  and moves horizontally at a velocity  $U$ . The bottom wall is fixed and has a lower temperature  $T_0$ . If the distance between these two walls is  $H$ , it gives an analytic solution for the normalized temperature at steady state

**Table 2**  
Computational cost of the implicit UGKS and the explicit UGKS for Sod test case at  $Kn = 10$  with different time steps.

	Explicit UGKS	IUGKS- $\epsilon'$ with $\epsilon = 0.75$			
CFL number	0.5	50	200	400	800
CPU time (sec)	4405.4	270.4	77.7	46.0	29.8
Speedup	1.0	16.3	56.7	95.8	147.7

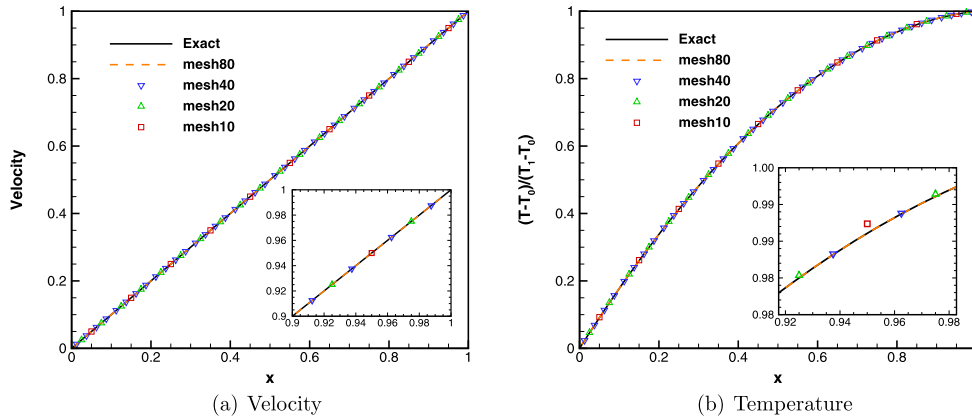


**Fig. 8.** The normalized velocity and temperature distributions obtained on different meshes by IUGKS with  $\tau = 0.001\Delta t_s$ .

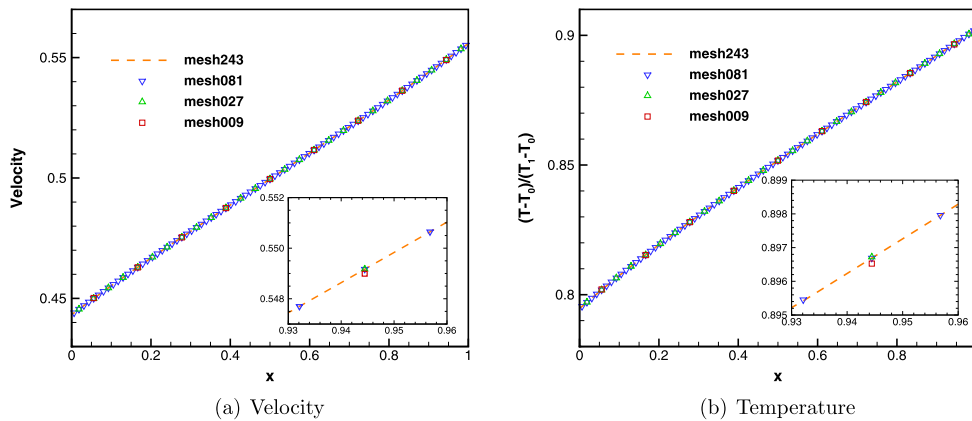


**Fig. 9.** The normalized velocity and temperature distributions obtained by IUGKS on different meshes at  $Kn = 10$ .

$$\hat{T}_e(y) = \frac{T - T_0}{T_1 - T_0} = \frac{y}{H} + \frac{PrEc}{2} \frac{y}{H} \left(1 - \frac{y}{H}\right) \tag{43}$$

where  $Ec = U^2/C_p(T_1 - T_0)$  is the Eckert number, and  $C_p$  is the specific heat ratio at constant pressure.

In this case we use  $T_1 = 274$  K,  $T_0 = 273$  K, and  $U = 30$  m/s for the incompressible limit. The argon gas with molecular mass  $m_0 = 6.63 \times 10^{-26}$  kg is employed, and  $Ec \approx 1.73$ . Uniform meshes with 10, 20, 40 and 80 discrete cells are used. The results obtained by the IUGKS with  $\tau = 0.001\Delta t_s$  in continuum regime are plotted in Fig. 8.

The errors of  $L_2$  norms are calculated by

$$E_{L_2} = \frac{\|y(x) - y_e(x)\|_2}{\|y_e(x)\|_2}, \tag{44}$$

where  $y(x)$  denotes numerical distribution of a specific flow variable, and  $y_e(x)$  is the corresponding exact solution. For this case, a normalized temperature distribution is used to evaluate the errors. The  $L_2$  norms with respect to mesh size are plotted in Fig. 10(a). It can be seen that the IUGKS has a second-order accuracy in space for the continuum flow.

In order to measure the spatial convergence of the IUGKS in rarefied regime, the same case at  $Kn = 10$  is computed on a group of meshes of 9, 27, 81 and 243 cells. The results are given in Fig. 9. Since there is no analytic solution for the Couette flow in rarefied regime, a relative method to measure the error is adopted, i.e.,

$$E_{L_2} = \frac{\|y_c(x) - y_f(x)\|_2}{\|y_f(x)\|_2}, \tag{45}$$

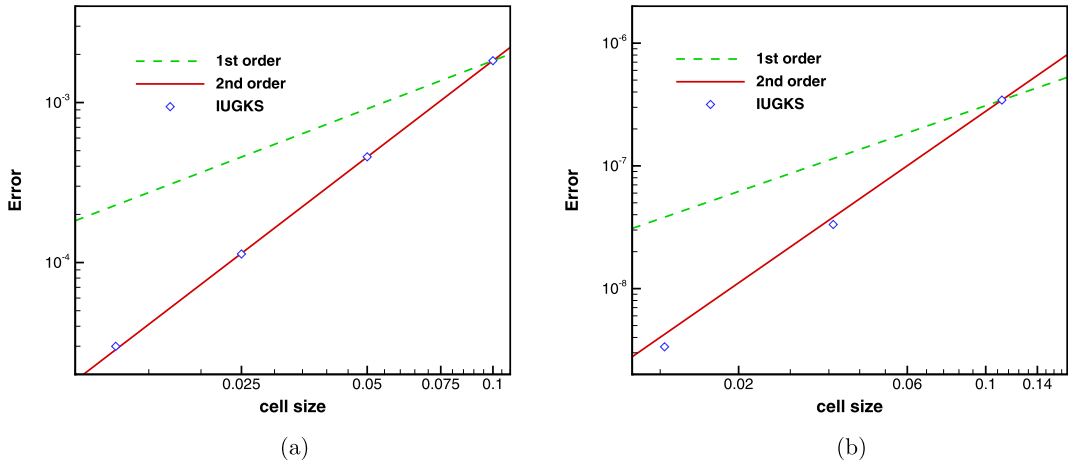


Fig. 10. Spatial accuracy of the IUGKS for (a)  $\tau = 0.001\Delta t_s$  in continuum flow, and (b)  $Kn = 10$  in rarefied flow.

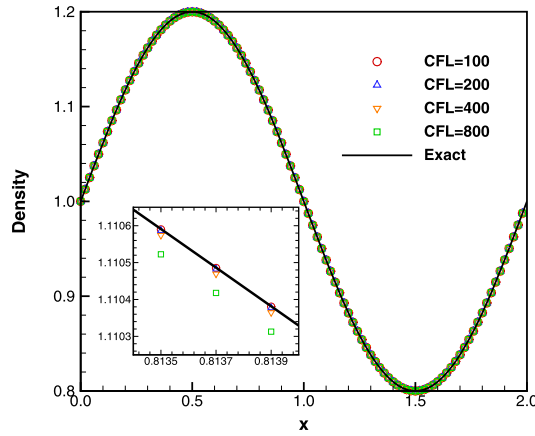


Fig. 11. The density distribution at time  $t = 2$  obtained by the IUGKS with different time steps.

where  $y_c(x)$  and  $y_f(x)$  are the numerical solutions on the coarse and the fine meshes, respectively. The results given in Fig. 10(b) show that a second-order accuracy in space can be obtained as well for the case in the collisionless limit.

### 3.3. Advection of density perturbation

In order to test the temporal accuracy of the IUGKS for unsteady flow simulations, the one-dimension case of advection of density perturbation [49] is employed. The initial condition is set as follows

$$\rho(x) = 1 + 0.2 \sin(\pi x), \quad U(x) = 1, \quad p(x) = 1, \quad x \in [0, 2]. \tag{46}$$

The periodic boundary condition is implemented and it gives an analytic solution

$$\rho_e(x, t) = 1 + 0.2 \sin(\pi(x - t)). \tag{47}$$

In the Euler limit, the UGKS is supposed to have an error on the order of  $\mathcal{O}(\Delta x^2, \Delta t^2)$ . When  $\mathcal{O}(\Delta t^2)$  is dominant, we can capture the convergence order of the IUGKS with respect to time step. Therefore, in this case we adopt a very fine uniform mesh with 10000 cells and use relatively large time steps. A small mean collision time  $\tau = 0.001\Delta t_s$  is used here to drive the IUGKS to get a continuum inviscid solution.

Fig. 11 shows the density distribution at time  $t = 2$  that obtained by the IUGKS with different time steps. It can be predicted that the IUGKS with  $\epsilon = 0.5$  for the C-N temporal discretization has a second-order accuracy in time because it has been proved that the IUGKS can automatically reduce to the second-order accurate explicit UGKS for small time step cases. In order to further validate this, the errors for different time step cases are calculated by Eq. (44) to measure the temporal accuracy of the IUGKS. From Fig. 12(a), it shows that the C-N scheme with  $\epsilon = 0.5$  achieves the expected temporal accuracy. The accuracy of IUGKS with a temporal discretization of  $\epsilon = 0.75$  has also been tested, see in Fig. 12(b). As expected, the IUGKS for the case with  $\epsilon > 0.5$  has a first-order accuracy in time.

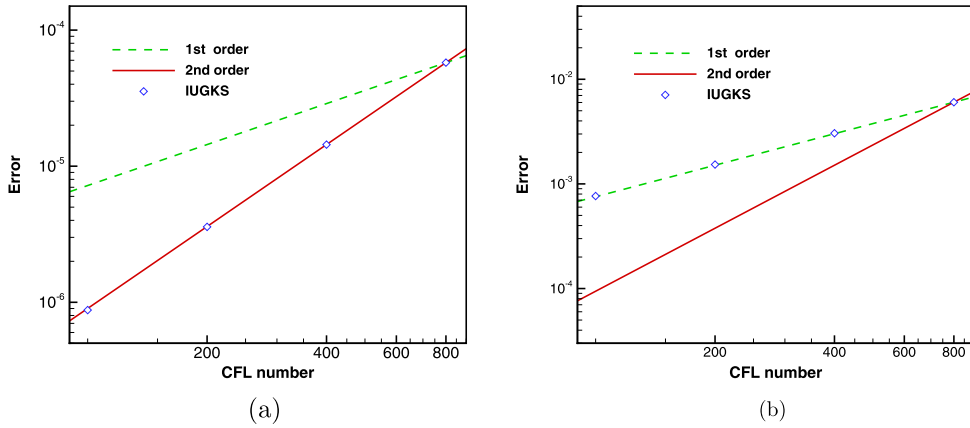


Fig. 12. Temporal accuracy of the IUGKS with (a)  $\epsilon = 0.5$  and (b)  $\epsilon = 0.75$  measured by Eq. (44).

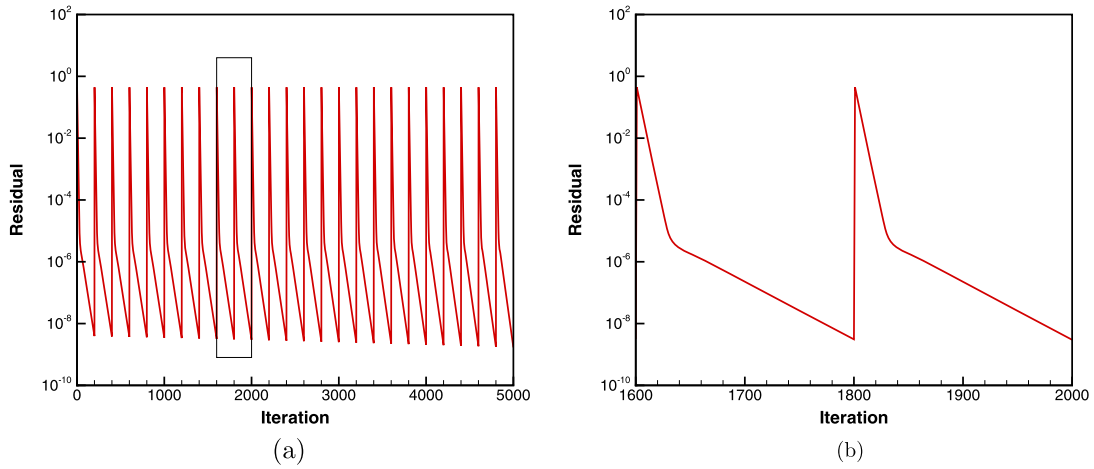


Fig. 13. Convergence history of the unsteady flow of sine wave propagation for the case at CFL = 400 with  $\epsilon = 0.5$ . (a) Residual variation with respect to total iteration steps; (b) enlargement for two evolution steps.

The convergence history of the unsteady flow of sine wave propagation is shown in Fig. 13. The given residual is evaluated by the  $L_2$  norm of the momentum component of Eq. (25), which measures the convergence of the first order moment of the Boltzmann model equation. For this case, we set the maximum inner iteration as 200. As shown in Fig. 13(a), for each evolution step the residual of the unsteady governing equation can be reduced to the order of  $10^{-8}$ , and the error of flow variable change for each evolution step is about  $10^{-12}$ . Usually, there is no need to constrain the residual of each evolution step to such a small value. Considering the temporal accuracy of numerical scheme, a residual of  $\mathcal{O}(\Delta t^m)$  for each step is sufficient, where  $m$  is the order of temporal accuracy. In practice, two or three orders of residual reduction is acceptable [27]. The details of the converge history in two time-marching steps are enlarged in the Fig. 13(b), where it gives a typical convergence curve. Specifically, the high-frequency error can be more efficiently eliminated by the iterations than the low-frequency error. After the high-frequency error is mainly eliminated, the convergence rate will decrease and more iterations are required for low-frequency error. The multigrid method [2,50] could be adopted to further improve the convergence property for a higher efficiency.

In addition, based on this periodic case we further investigate the accuracy of the IUGKS in different flow regimes. The time accuracy tests are applied in the cases at  $Kn = 0.001, 0.01, 0.1, 1$  and 10 on a uniform mesh with 400 cells. The errors measured by Eq. (45) are plotted in Fig. 14 with respect to the time step. The IUGKS achieves second order accuracy for all cases from continuum to free molecular flows.

Generally, the stability of IUGKS can be achieved by adjusting the parameter  $\epsilon$  so that the IUGKS is able to evolve in time using any large time step. However, large time steps may lead to unsatisfactory results due to the decrease of time accuracy. Even though large time steps are permissible, the time resolution of physical solutions should be considered. In order to explore the applicability of the IUGKS, we utilize this periodic case on a uniform mesh with 100 cells to further investigate the scheme. In Fig. 15(a), we give the results obtained with different time steps, i.e.,  $\Delta t = T/20, T/10, T/5$  and  $T/2$ , where  $T = 2$  is the period of this sine wave. With respect to the wave length, the relative error of the location of extremum value is about 0.8%, 3%, 10.8 and 36.1%. From Fig. 15(a), it can be found that the shape of the sine wave is well preserved even

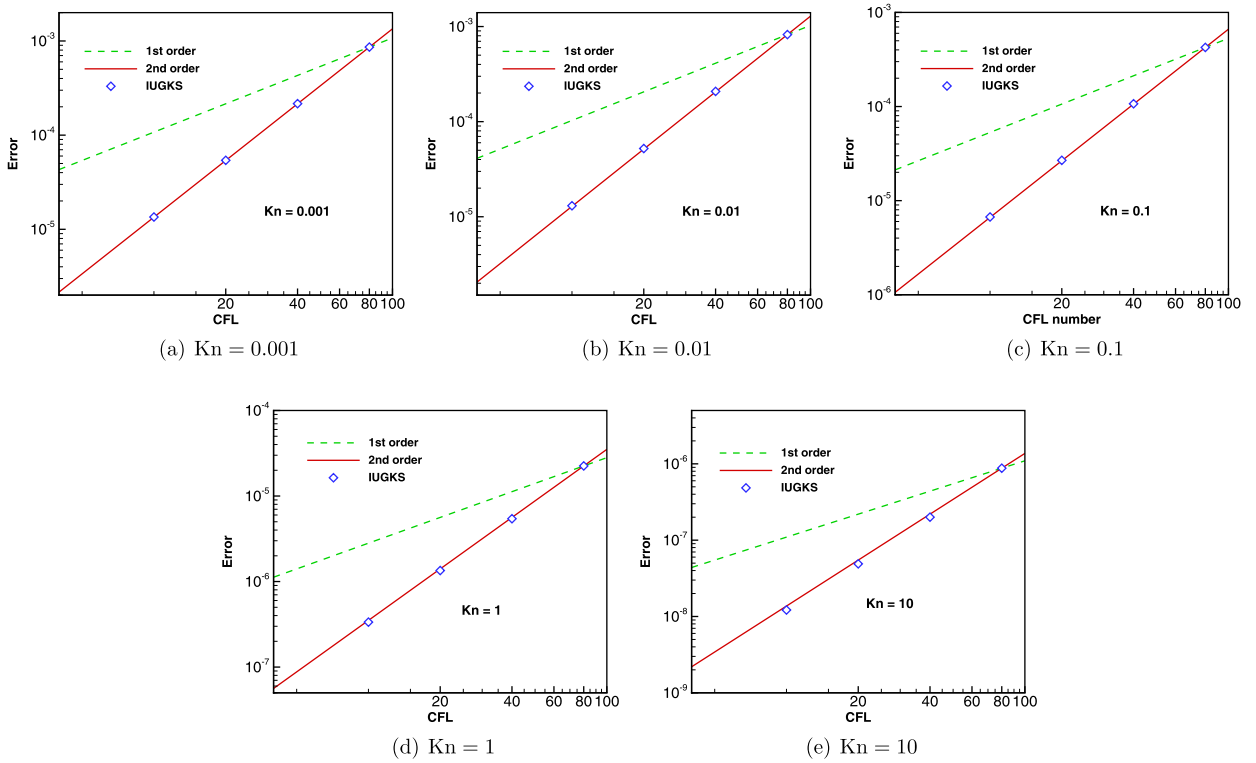


Fig. 14. Accuracy test of the IUGKS in different flow regimes.

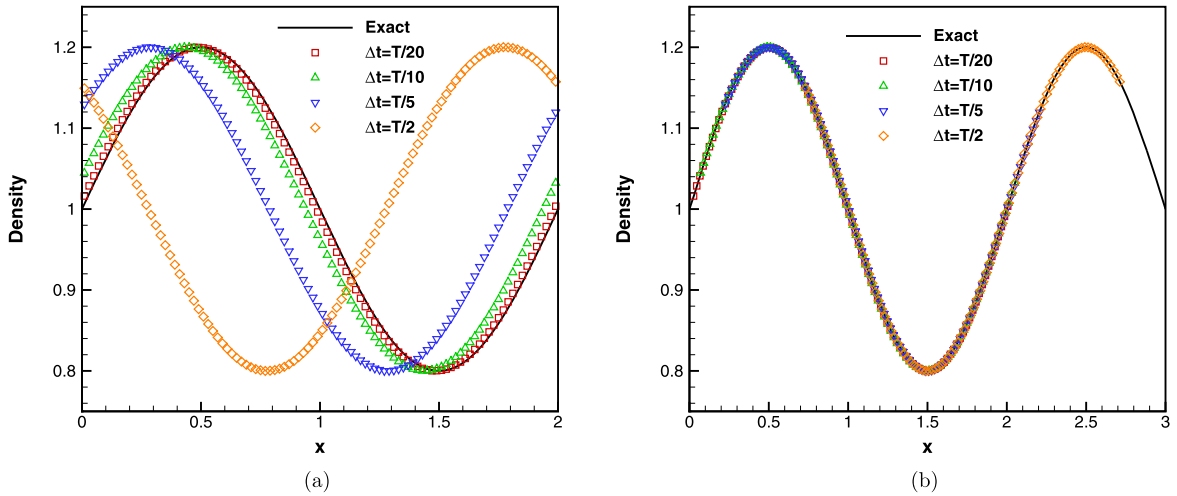


Fig. 15. Density distribution obtained with  $\Delta t = T/20, T/10, T/5$  and  $T/2$ . (a) Phase error and (b) shifted results.

for the case with  $\Delta t = T/2$ , and the solutions can coincide to the exact one after a shift, see Fig. 15(b). Based on this case, we can roughly draw a conclusion that considering the requirement on time accuracy, in order to capture the flow variable evolution, the numerical time step chosen to evolve the unsteady flow field should not be larger than one-tenth of the period of flow evolution.

### 3.4. Rayleigh flow

The Rayleigh flow is an unsteady gas flow around a vertical plate with infinite length. Initially, the argon gas with molecular mass  $m_0 = 6.63 \times 10^{-26}$  kg is stationary and has a temperature of 273 K, and suddenly the plate obtains a constant vertical velocity of 10 m/s with a higher temperature of 373 K. The computational domain is 1 m long, which is

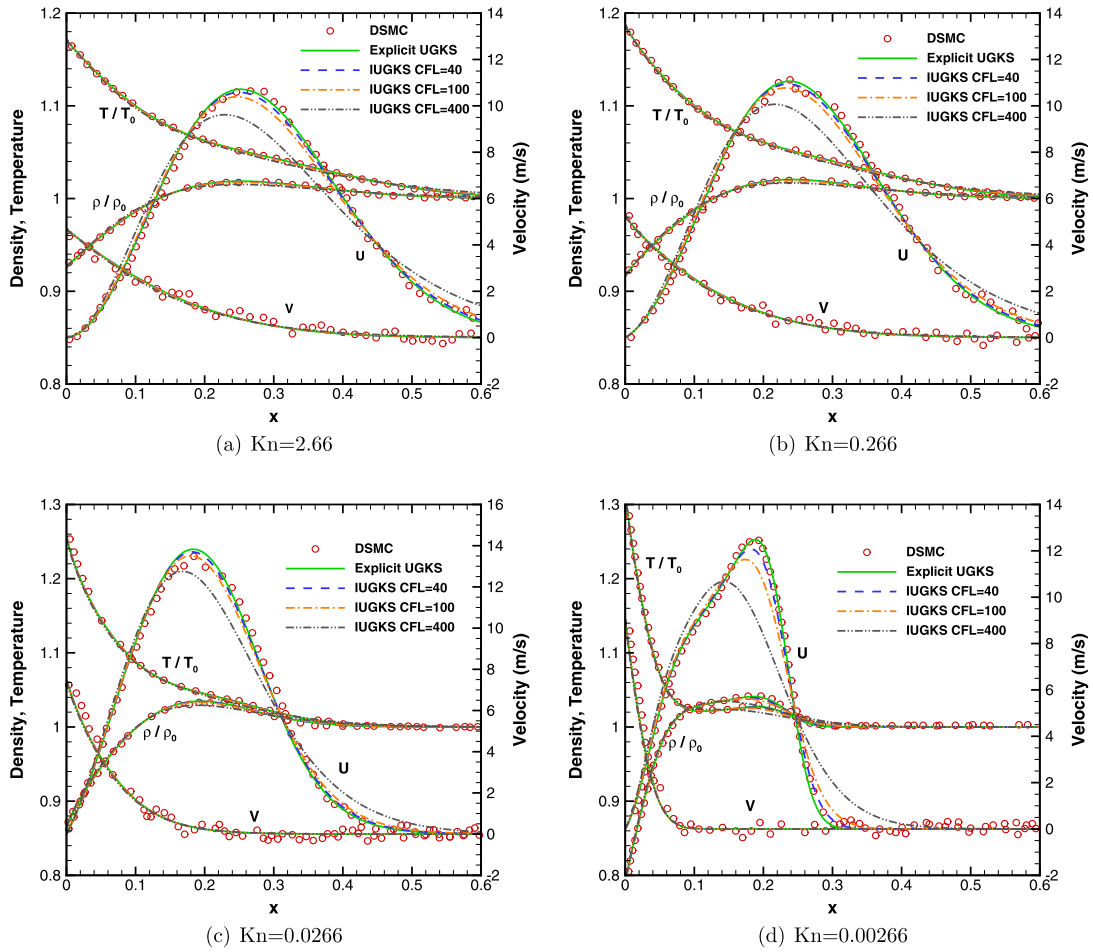


Fig. 16. Rayleigh problems at different Knudsen numbers which cover the free molecular, transition and continuum regimes. IUGKS here denotes the IUGKS- $\epsilon'$  with  $\epsilon = 0.75$ .

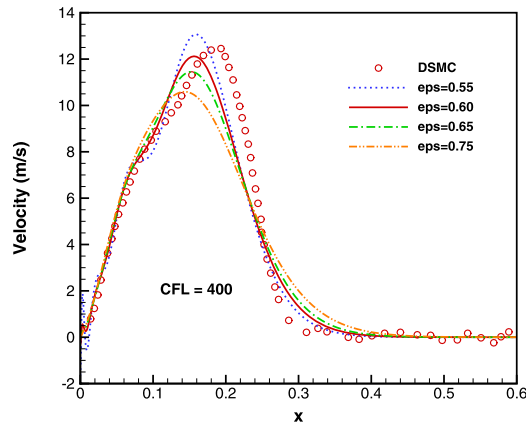


Fig. 17. Rayleigh problems at  $Kn = 0.00266$  and  $CFL = 400$  with different  $\epsilon$ .

the characteristic length to define the Knudsen number  $Kn$  by the variable hard sphere (VHS) model. The dynamic viscosity is computed by  $\mu = \mu_0(T/T_0)^\omega$  with  $\omega = 0.81$ . Results at time  $t = 0.7$  ms are discussed here.

The target of the IUGKS is to release the time step restriction from small-size cells on non-uniform mesh and thus to accelerate overall computational efficiency. For this test, we employ non-uniform mesh with the minimum cell size of 0.0005 m near the plate. The results at different Knudsen numbers are plotted in Fig. 16, where the density and temperature are normalized by  $\rho_0$  and  $T_0$ . In comparison with the DSMC results obtained from the reference paper [18] and those from

**Table 3**  
Computational cost for Rayleigh Problem with different time steps.

	Kn	Explicit UGKS	IUGKS- $\epsilon'$ with $\epsilon = 0.75$			
		CFL = 0.5	40	100	400	1200
CPU time (min)	2.66	437.8	22.5	10.3	4.0	1.9
	0.266	435.0	25.9	11.5	4.8	1.8
	0.0266	436.7	31.0	14.3	7.1	3.3
	0.00266	439.8	48.2	28.2	13.7	11.1
Speedup	2.66	1.0	19.5	42.3	108.7	236.6
	0.266	1.0	16.8	37.7	91.0	236.8
	0.0266	1.0	14.1	30.6	61.1	132.4
	0.00266	1.0	9.1	15.6	32.1	39.5

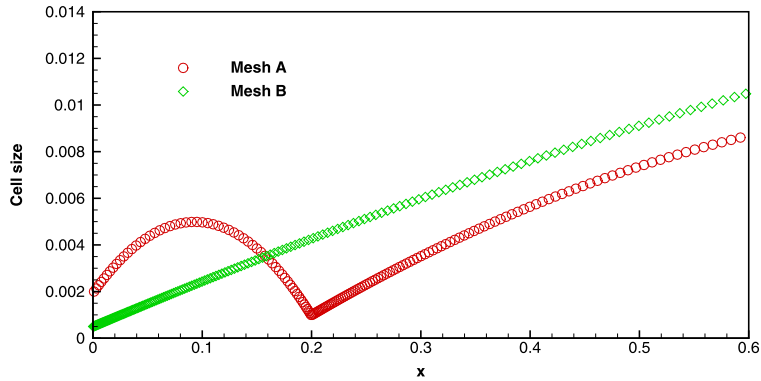


**Fig. 18.** The distribution of the cell size used in simulation of Rayleigh problems. (For interpretation of the colors in the figure(s), the reader is referred to the web version of this article.)

the explicit UGKS simulation, IUGKS- $\epsilon'$  with  $\epsilon = 0.75$  can give satisfactory results with a relatively large time step. With a continuous increment of time step, the solutions gradually deviate from the reference ones due to the increase of temporal discretization error. As analyzed in Sec 3.3, the time step should not be larger than one tenth of the wave period. For the case with CFL = 400, the time step is about one seventh of the evolution time. If we use a smaller  $\epsilon$  to increase the temporal accuracy, we can obtain better results, see in Fig. 17. It is noticed that for this small Knudsen number case, small  $\epsilon$  may give oscillatory solution due to the initial discontinuity at the solid wall. This has also been analyzed in Sec 3.1. The collisionless limit requires the interval of discrete velocities to satisfy  $\Delta u \sim \Delta x/t$ . In order to get smooth solutions, we use 600 velocity points uniformly in  $u$ -direction and 100 points in  $v$ -direction to cover a range from  $-2023$  m/s to  $2023$  m/s. Extra more discrete points have been employed for discretization of the physical and velocity space in this case so that it gives more reliable results in the efficiency testing due to long program running time. We present the computational cost in Table 3 at different Knudsen numbers with various time steps. Generally more inner iterations are required in the small Knudsen number case. The increase of computational efficiency for near continuum flows is not as much as that in rarefied cases, but it is still about ten times faster than that of the explicit scheme with CFL = 40. Since the IUGKS with  $\epsilon = 0.75$  is stable enough, we also give the computational cost for case with CFL = 1200 as a reference even though the solutions under such a condition may not make any sense for a satisfactory solution.

In order to check the sensitivity of the IUGKS to the mesh size, the Rayleigh problems are computed on two kinds of meshes, whose cell size distributions are given in Fig. 18. The mesh denoted by the green diamonds is used in previous calculations, and the one denoted by red circles has a cell size shrinking at  $x = 0.2$  m. Comparisons between results obtained from these two meshes are given in Fig. 19, from which it can be observed that flow can efficiently spread through the small cell size region, and identical solutions to the previous ones can be obtained. A fixed time step  $\Delta t = 8.9 \mu\text{s}$  is used which is equivalent to the previous case with CFL = 40 shown in Fig. 16.

### 3.5. Wall bounded Rayleigh flow

The Rayleigh problems tested in Section 3.4 are one-dimensional, where periodic boundary conditions are imposed in the  $y$ -direction. Here we add two parallel solid walls along  $x$ -direction at two locations separated by 1 m in the  $y$ -axis, which restrict the movement of the flow in the vertical direction. The schematic for the setting is shown in Fig. 20. The lower and upper solid walls have a length of 4 m and a constant temperature of  $T_{wall} = 273$  K. The argon gas has molecular mass  $6.63 \times 10^{-26}$  kg, which corresponds to a specific gas constant of  $R = 208.13$  J/(kg · K). The initial gas temperature is  $T_0 = 273$  K. The side plates move vertically at 10 m/s with a higher temperature of 373 K. The Maxwellian diffusive

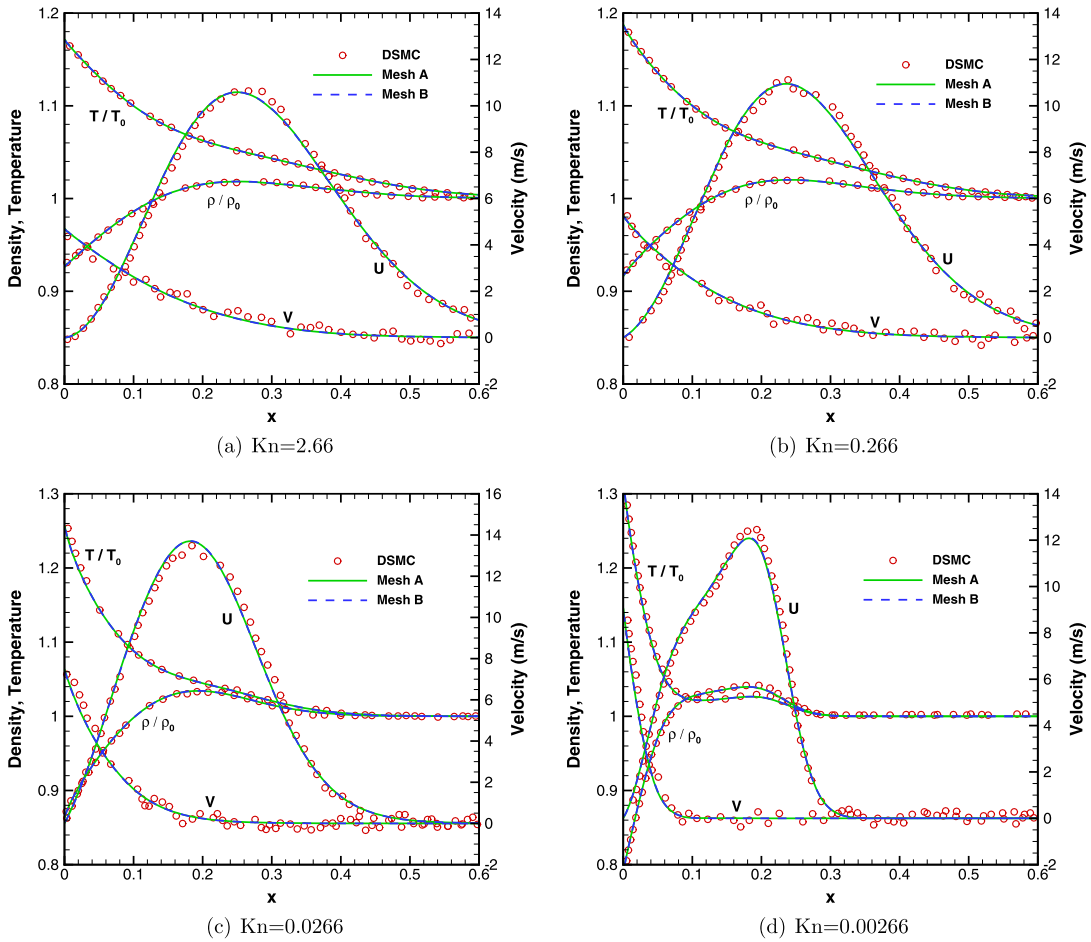


Fig. 19. Comparison of the results for Rayleigh problems computed on different meshes with a fixed time step  $\Delta t = 8.9 \mu s$ .

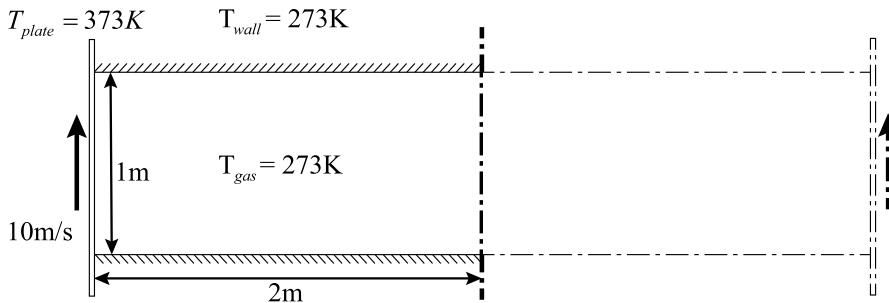


Fig. 20. The schematic for wall bounded Rayleigh flow.

boundary condition is imposed on the solid isothermal walls. In addition, symmetric boundary condition is imposed at  $x = 2 \text{ m}$ , so that half domain can be used in computation. The case of  $Kn = 0.05$  is considered here.

In order to check the convergence of solutions with respect to the cell size and the time step, numerical simulations are carried out on different meshes using different time steps. The spatial discretizations used in the test case are  $11 \times 21$ ,  $21 \times 41$ ,  $41 \times 81$  and  $81 \times 161$ . In the following, these meshes will be denoted by  $N = 11$ ,  $N = 21$ ,  $N = 41$  and  $N = 81$  for simplicity, where  $N$  means the number of discrete cells along the vertical plate. In this case, the non-dimensional time and time step are used, and the normalization is based on a reference time scale  $t_0 = L_0/U_0$ , where  $L_0 = 1 \text{ m}$  and  $U_0 = \sqrt{2RT_0}$ . The time steps used in these cases for the IUGKS are  $\Delta t = 0.01$ ,  $0.05$  and  $0.1$ . As references, the cases with  $\Delta t = 0.001$  are computed as well using the explicit UGKS. Flow variables along the central vertical and horizontal lines ( $x = 1 \text{ m}$  and  $y = 0.5 \text{ m}$ ) at  $t = 1.5$  are monitored to illustrate the mesh convergence solutions of the unsteady flow, where the results are plotted in Fig. 21 and Fig. 22. It shows that the results on the mesh of  $N = 41$  have little difference from those on the

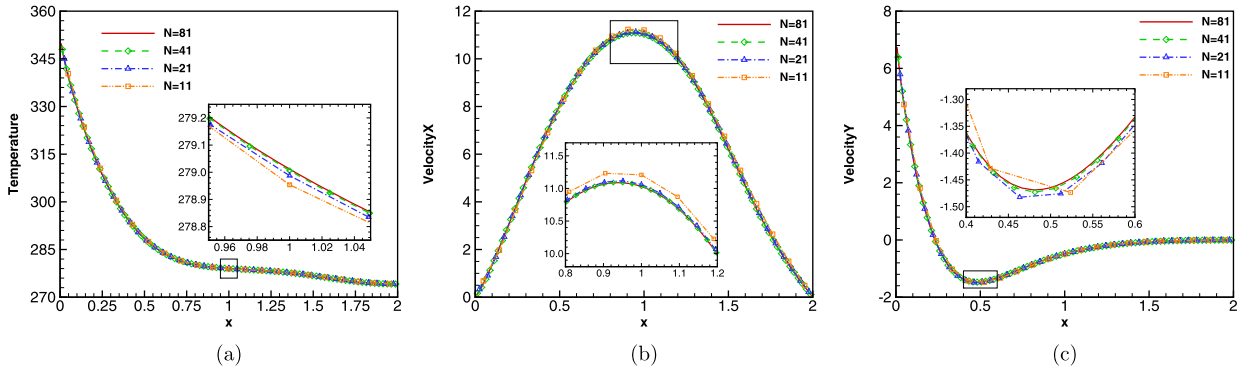


Fig. 21. Flow variables along the central horizontal line obtained on different meshes.  $N$  denotes the discrete cell number along the vertical plate.

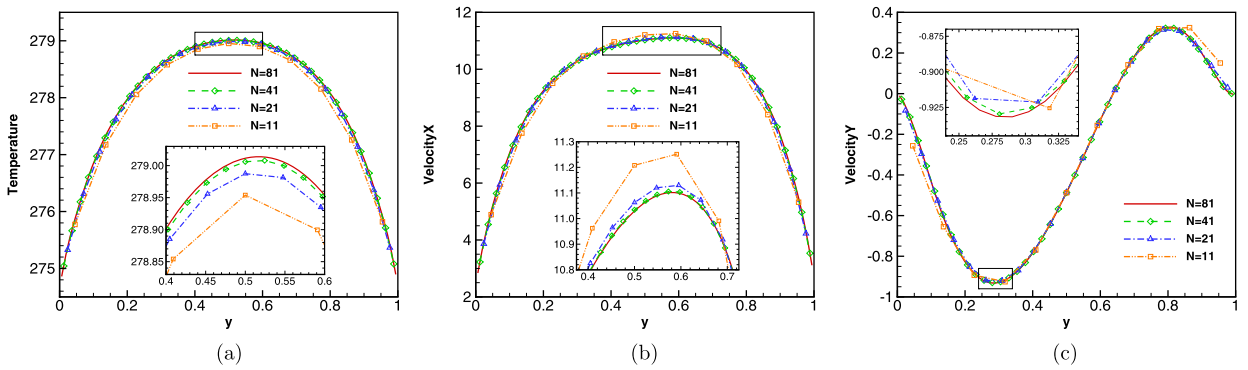


Fig. 22. Flow variables along the central vertical line obtained on different meshes.  $N$  denotes the discrete cell number along the vertical plate.

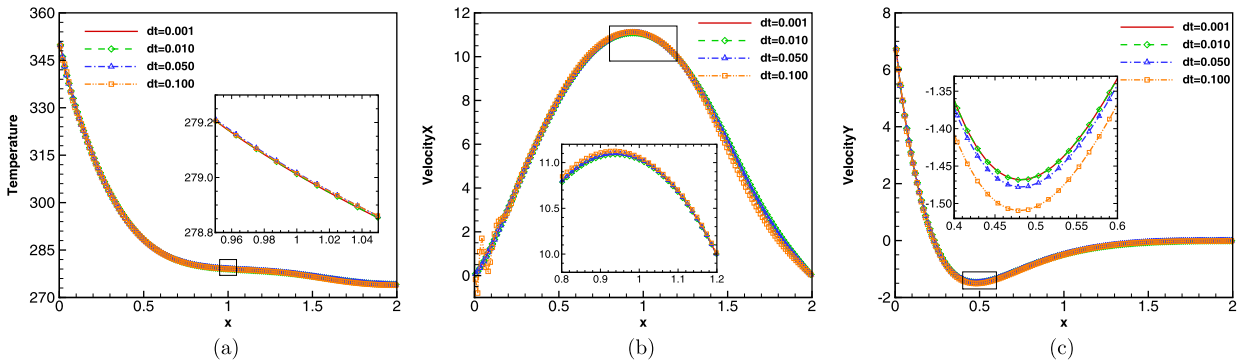


Fig. 23. Flow variables along the central horizontal line obtained with different time steps.

mesh of  $N = 81$ , which can be regarded as a mesh convergent solution. Flow variables along central lines obtained using different time steps are given in Fig. 23 and Fig. 24 which show the convergence of the evolving solutions with respect to different numerical time steps.

The flow variables such as magnitude of velocity and temperature at different times are plotted in Fig. 25 and Fig. 26, which clearly present the flow evolution. The mechanism for the flow evolution comes from plate's shearing and thermal heating effect. Based on the data on the central lines, the rarefied gas effect appears, such as the velocity slip and temperature jump near the solid walls.

The surface quantities, such as pressure, shear stress and heat flux at four different instants are given in Fig. 27, Fig. 28 and Fig. 29. Detailed data for this case at points along the central lines and on the solid walls at time  $t = 1.5$  have been listed in Tables A.4–A.8.

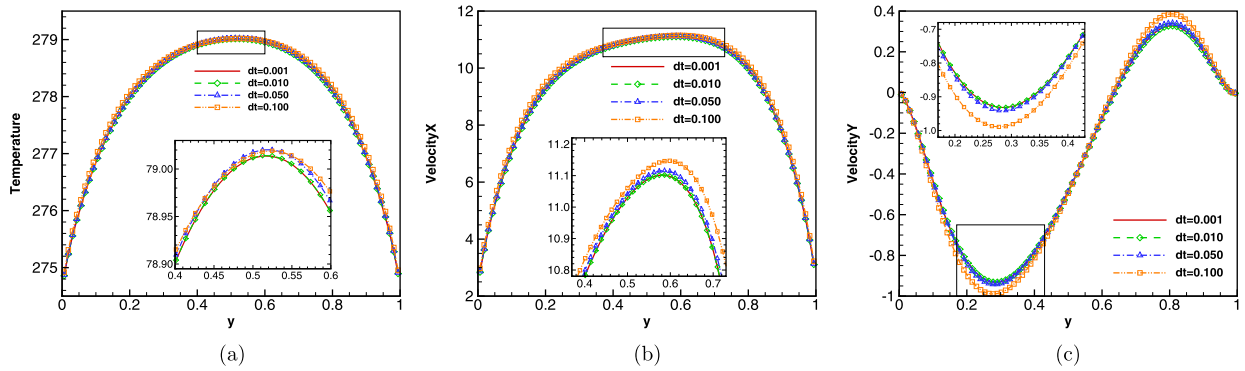


Fig. 24. Flow variables along the central vertical line obtained with different time steps.

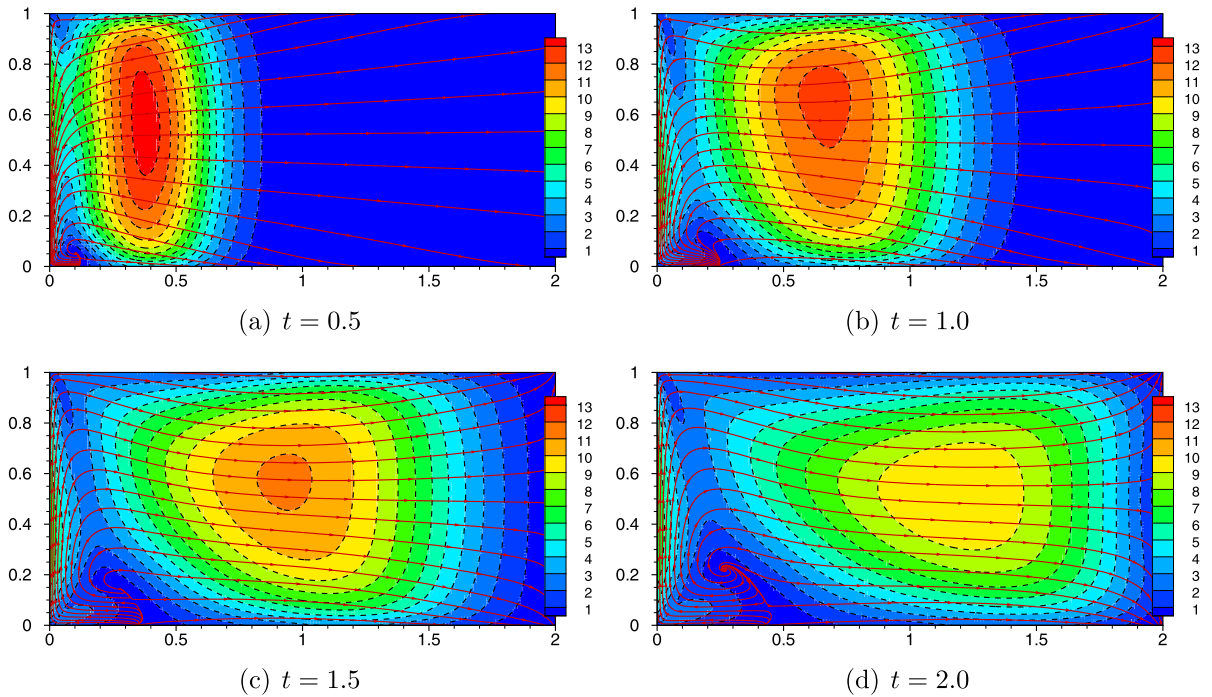
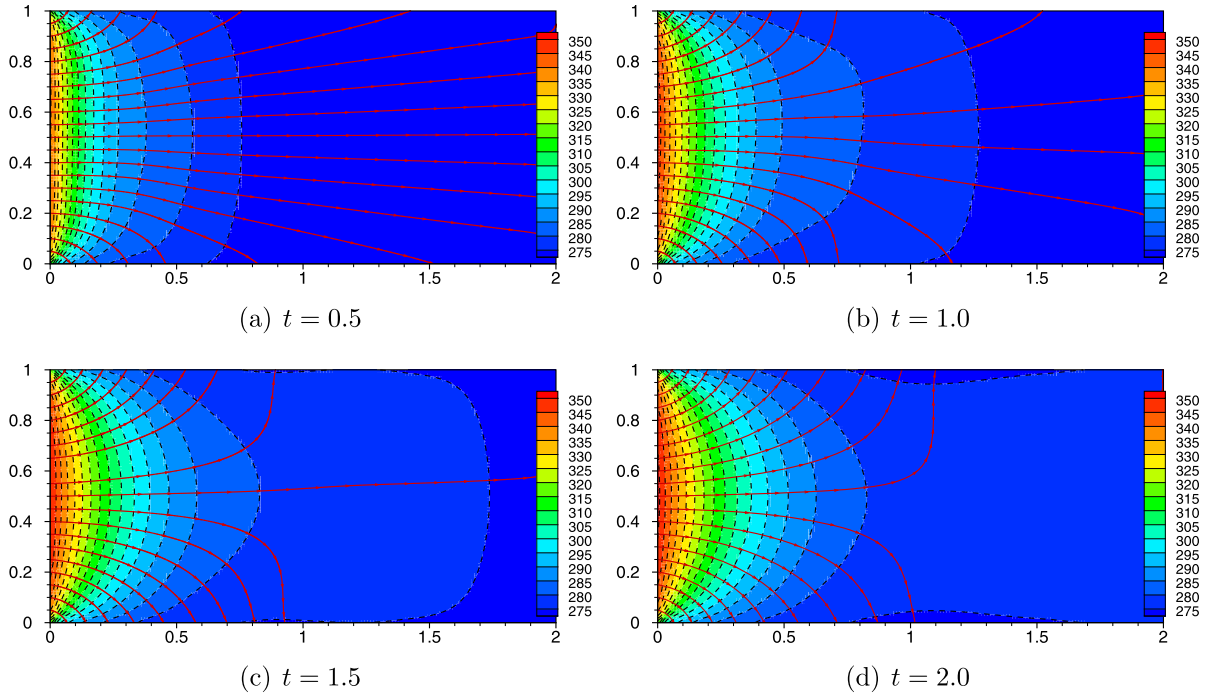


Fig. 25. Magnitude of velocity distribution for wall bounded Rayleigh flows at different times. Background: explicit UGKS with  $\Delta t = 0.001$ ; dotted line: IUGKS with time step  $\Delta t = 0.01$ ; red solid line: streamlines.

### 3.6. Hypersonic flow past a square cylinder

This high-speed rarefied flow past a square cylinder is computed to validate the efficiency and stability of the current implicit scheme. The freestream is hypersonic flow of the argon gas at a Mach number 5 with a temperature of  $T_\infty = 273$  K. The computational domain is  $[-0.06 \text{ m}, 0.08 \text{ m}] \times [-0.06 \text{ m}, 0.06 \text{ m}]$ , and the square center locates at the origin. The spatial discretization is the same as that described in [51]. The density in the freestream is  $8.58 \times 10^{-5} \text{ kg/m}^3$ , resulting in a global Knudsen number 0.1 which is defined with respect to the square side length 0.01 m. The dynamic viscosity is calculated by  $\mu = \mu_0(T/T_0)^\omega$  where  $\omega = 0.81$ .

The density, pressure and velocity distributions at the steady state are given in Fig. 30, where the results obtained from the IUGKS are compared with those from the DSMC method. Generally, the IUGKS results agree well with the DSMC data. For the velocity along  $y$ -direction, the IUGKS gives a straight line on the symmetric plane for the zero contour line while the DSMC gives some noises in the freestream due to the statistic error. The surface quantities, such as pressure, shear stress, and heat flux on the upper half walls of the cylinder are given in Fig. 31 and compared with the DSMC data. Good agreement has been obtained. For unsteady flow simulation, we show the time evolution of the temperature distribution at several instants in Fig. 32 to illustrate the capability of the IUGKS for capturing time-dependent evolution solutions.



**Fig. 26.** Temperature distributions for wall bounded Rayleigh flows at different times. Background: explicit UGKS with  $\Delta t = 0.001$ ; solid line: IUGKS with time step  $\Delta t = 0.01$ ; red solid line: heat flux.

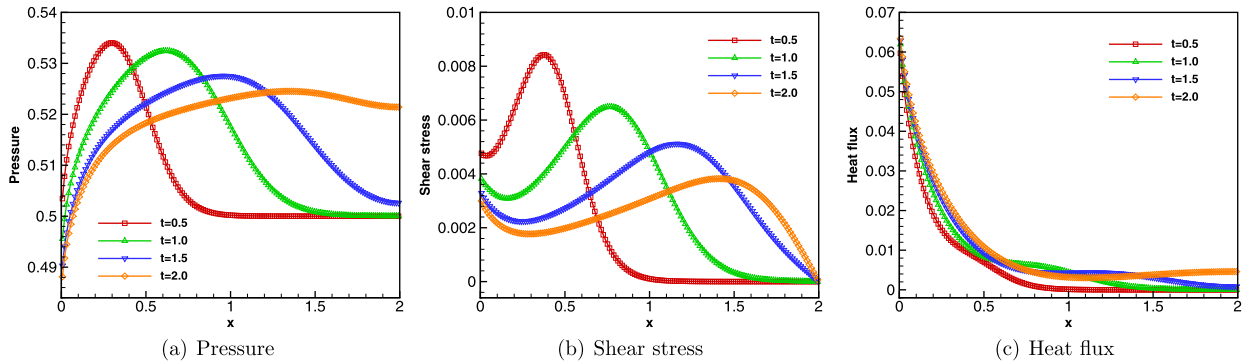


**Fig. 27.** Surface quantities along the lower wall changing with time. The pressure and shear stress are normalized by  $\rho_0 C_0^2$  where  $C_0 = \sqrt{2RT_0}$ , and the heat flux is normalized by  $\rho_0 C_0^3$ .

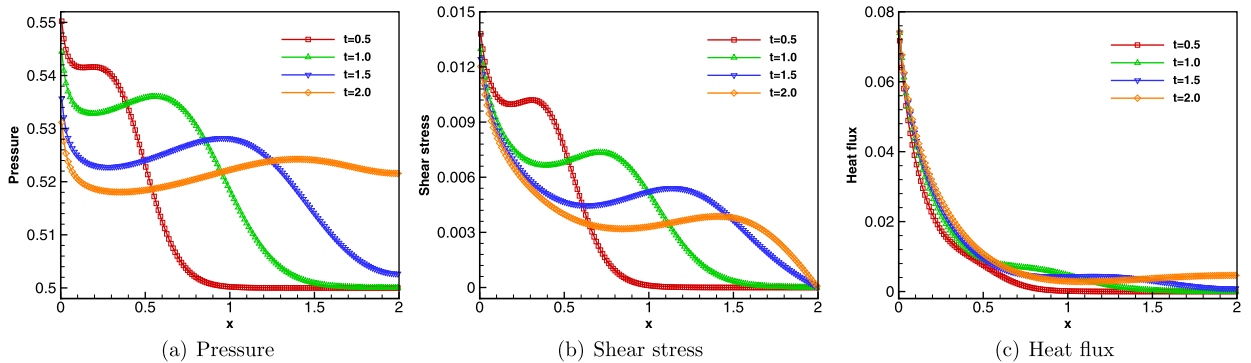


**Fig. 28.** Surface quantities along the upper wall changing with time. The pressure and shear stress are normalized by  $\rho_0 C_0^2$  where  $C_0 = \sqrt{2RT_0}$ , and the heat flux is normalized by  $\rho_0 C_0^3$ .

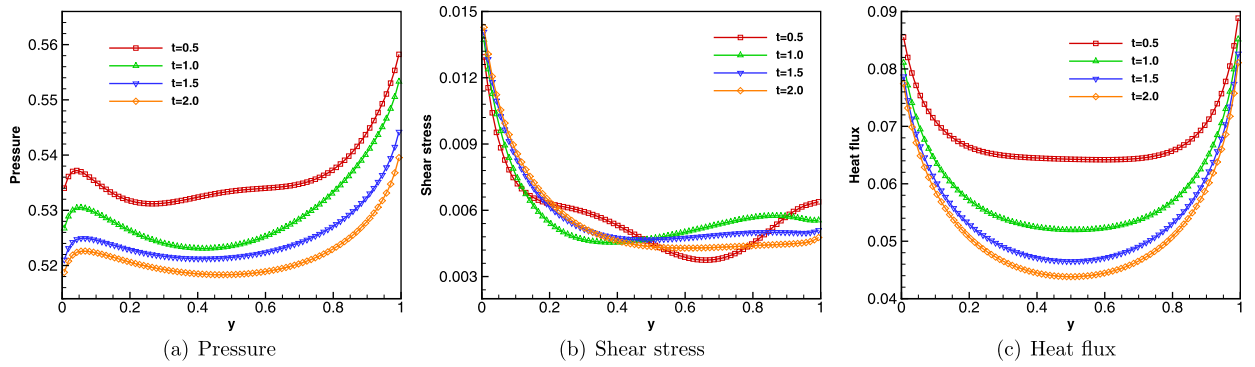


**Fig. 29.** Surface quantities along the side plate changing with time. The pressure and shear stress are normalized by  $\rho_0 C_0^2$  where  $C_0 = \sqrt{2RT_0}$ , and the heat flux is normalized by  $\rho_0 C_0^3$ .

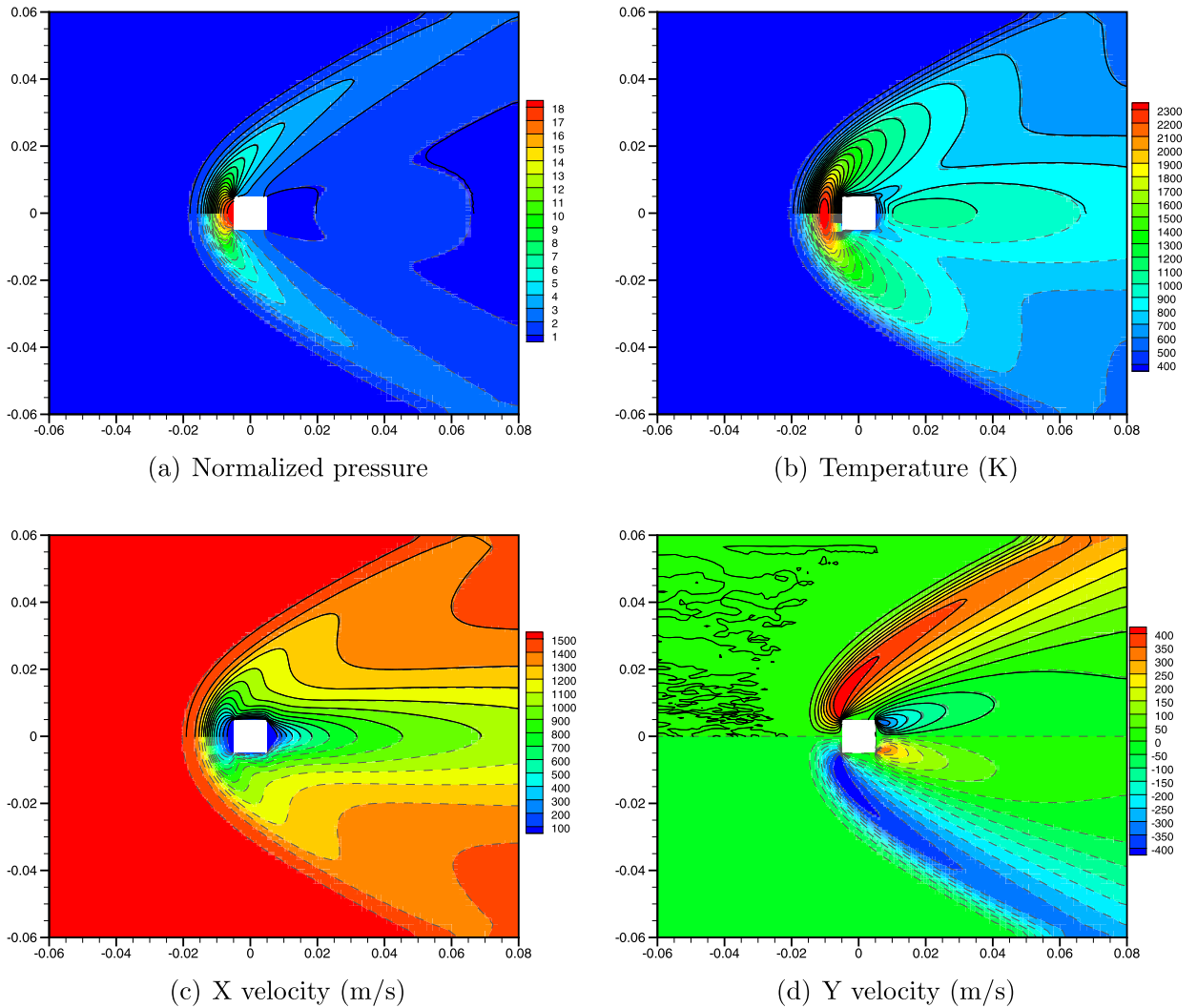


**Fig. 30.** Flow variable distributions at steady state for hypersonic flow past a square cylinder at  $Ma = 5$  and  $Kn = 0.1$ . The background with dashes lines present the results from the IUGKS, and solid lines in the upper half domain denote the DSMC results.

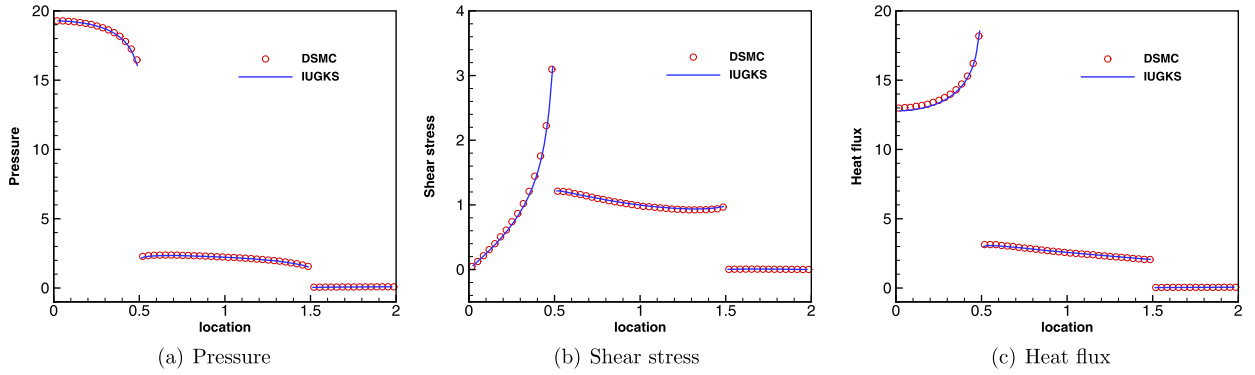


**Fig. 31.** Surface quantities on the upper half walls of the square cylinder. The pressure and shear stress are normalized by  $\rho_0 c_0^2$  where  $c_0 = \sqrt{2RT_0}$ , and the heat flux is normalized by  $\rho_0 c_0^3$ .

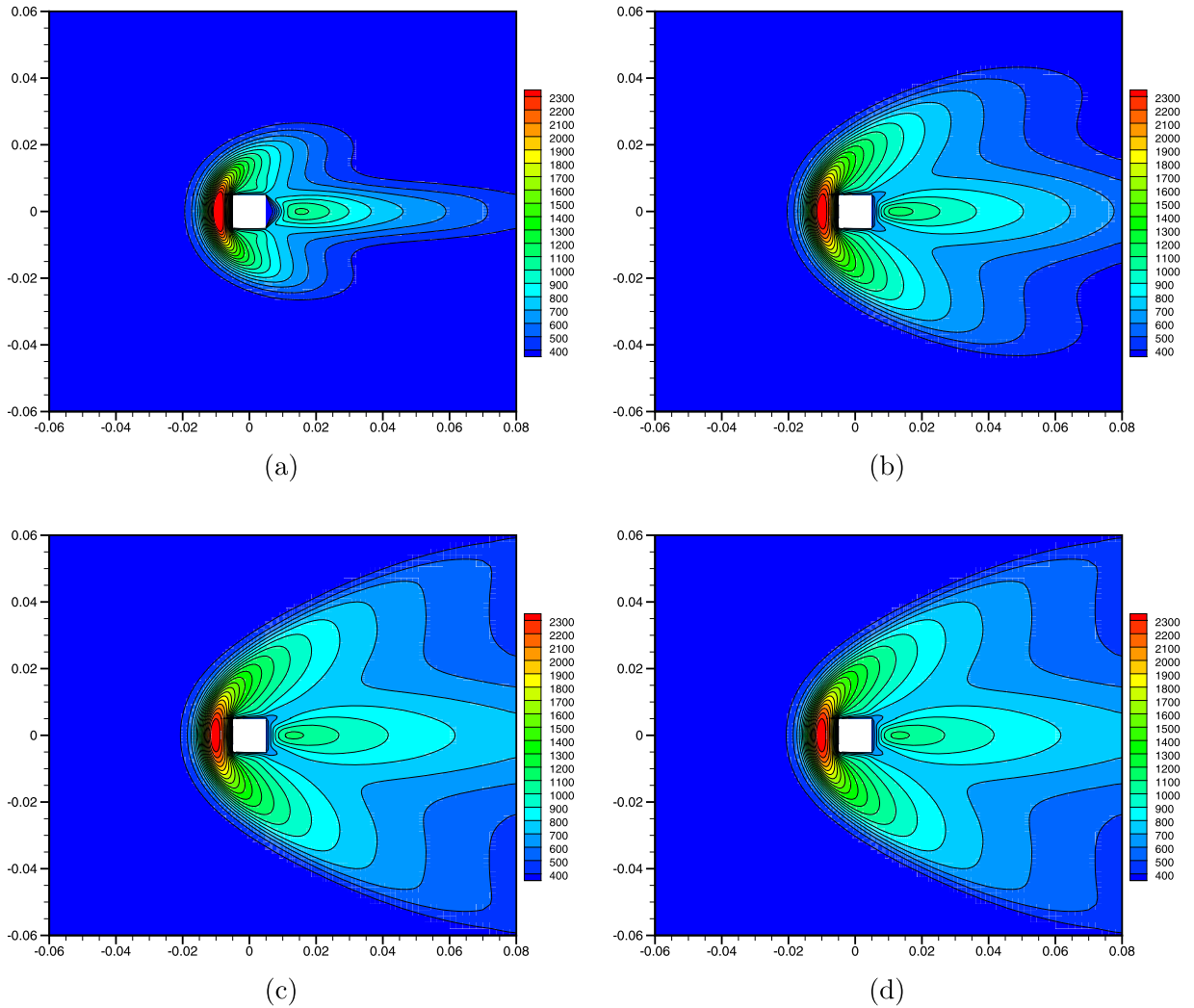


**Fig. 32.** Temperature distributions at different times for hypersonic flow past a square cylinder at  $Ma = 5$  and  $Kn = 0.1$ ; (a)  $t = 31.9 \mu s$ , (b)  $t = 63.8 \mu s$ , (c)  $t = 95.7 \mu s$  and (d)  $t = 127.6 \mu s$ .

**Table A.4**Flow variables along the horizontal central line at  $t = 1.5$  for wall bounded Rayleigh flow at  $Kn = 0.05$ .

$x$ (m)	$\rho/\rho_0$	$U$ (m/s)	$V$ (m/s)	$T$ (K)
6.2111801e-03	8.18016026e-01	7.85891e-02	6.74227e+00	3.49874e+02
1.3043478e-01	8.78648941e-01	1.86343e+00	2.03063e+00	3.24664e+02
2.5465838e-01	9.25634041e-01	4.07566e+00	-3.24820e-01	3.08005e+02
3.7888199e-01	9.63532054e-01	6.21682e+00	-1.29129e+00	2.96121e+02
4.7826087e-01	9.86728280e-01	7.73843e+00	-1.46834e+00	2.89537e+02
5.5279503e-01	1.00006841e+00	8.72092e+00	-1.41336e+00	2.86018e+02
6.2732919e-01	1.01027031e+00	9.54374e+00	-1.27672e+00	2.83483e+02
7.5155280e-01	1.02150242e+00	1.05300e+01	-9.86511e-01	2.80891e+02
8.7577640e-01	1.02735866e+00	1.10240e+01	-7.09914e-01	2.79616e+02
9.3788820e-01	1.02882990e+00	1.10878e+01	-5.90787e-01	2.79261e+02
1.0372671e+00	1.02965450e+00	1.09349e+01	-4.30510e-01	2.78891e+02
1.1242236e+00	1.02909392e+00	1.05386e+01	-3.19135e-01	2.78640e+02
1.2484472e+00	1.02654205e+00	9.53798e+00	-1.99918e-01	2.78221e+02
1.3726708e+00	1.02231600e+00	8.05902e+00	-1.18435e-01	2.77604e+02
1.4968944e+00	1.01709842e+00	6.24463e+00	-6.56574e-02	2.76766e+02
1.6211180e+00	1.01186368e+00	4.35078e+00	-3.38440e-02	2.75818e+02
1.7453416e+00	1.00756617e+00	2.63935e+00	-1.63774e-02	2.74951e+02
1.8695652e+00	1.00481128e+00	1.23354e+00	-8.04907e-03	2.74348e+02
1.9937888e+00	1.00382149e+00	5.64568e-02	-5.51691e-03	2.74121e+02

**Table A.5**Flow variables along the vertical central line at  $t = 1.5$  for wall bounded Rayleigh flow at  $Kn = 0.05$ .

$y$ (m)	$\rho/\rho_0$	$U$ (m/s)	$V$ (m/s)	$T$ (K)
6.1728395e-03	1.04684423e+00	2.84048e+00	-1.02562e-02	2.74860e+02
1.2962963e-01	1.03715456e+00	7.87730e+00	-5.77711e-01	2.77250e+02
2.1604938e-01	1.03337308e+00	9.47163e+00	-8.65068e-01	2.78103e+02
2.9012346e-01	1.03133167e+00	1.02116e+01	-9.31617e-01	2.78548e+02
3.7654321e-01	1.02999141e+00	1.06908e+01	-8.34530e-01	2.78849e+02
4.7530864e-01	1.02951243e+00	1.09836e+01	-5.68704e-01	2.79000e+02
5.1234568e-01	1.02958102e+00	1.10483e+01	-4.43631e-01	2.79014e+02
5.8641975e-01	1.03011130e+00	1.11016e+01	-1.78284e-01	2.78972e+02
6.6049383e-01	1.03120727e+00	1.10072e+01	7.24708e-02	2.78822e+02
7.4691358e-01	1.03335834e+00	1.05529e+01	2.80216e-01	2.78453e+02
8.0864198e-01	1.03563223e+00	9.82787e+00	3.27270e-01	2.78005e+02
8.7037037e-01	1.03869504e+00	8.55994e+00	2.65045e-01	2.77341e+02
9.9382716e-01	1.04848214e+00	3.11158e+00	-3.31606e-03	2.74895e+02

The final steady state solution is obtained at the physical time  $t = 319 \mu\text{s}$ , which takes about 14 hours using a serial computation. In comparison with the DSMC method, for evolving the solution by the same amount of time, the IUGKS basically takes the same computational cost as DSMC, where the DSMC targets on the steady state solution and no sampling is conducted in the unsteady process. The IUGKS has no noise and doesn't need any additional sampling for unsteady solution. If only the final steady state solution is needed, a fully implicit with multigrid technique can be used in UGKS to get a much higher efficiency, where the UGKS may become hundreds times faster than DSMC [2].

#### 4. Discussions and conclusions

In this paper, an implicit unified gas-kinetic scheme (IUGKS) is proposed for unsteady flow simulations in all Knudsen number regimes. By solving the time-accurate implicit governing equations of macroscopic variables and the gas distribution function with inner iterations, the flow field can be updated with a large time step, which is no longer restricted by the CFL stability condition.

For unsteady flow simulation, non-uniform meshes are usually used in many practical engineering applications, such as very fine mesh for viscous flow near solid boundaries and the mesh around the airfoil tip. For the explicit scheme, due to the CFL condition the global time step can become very small, and multiscale UGKS can become a single scale kinetic solver. Since the UGKS employs the analytic solution of the kinetic relaxation model, the numerical flux covers different flow regimes with the variation of the ratio between the time step and the local mean collision time, i.e.,  $\Delta t_s/\tau$ . A uniform time step determined by the smallest cell size could make the UGKS flux converge to the particle free transport when  $\Delta t_s/\tau \leq 1$ . Consequently, a free particle transport dynamics will be used in the flux evaluation even for these cells with a much larger cell size away from the boundaries. Therefore, the multi-scale property of the UGKS is not fully utilized. In the current IUGKS, the implicit treatment releases the CFL time step constraint, and the flow field can be updated by a numerical time step which is much larger than the global minimum one. In other words, for the unsteady flow with a large variation of cell size the flow dynamics in different regions can be settled to different flow regimes by IUGKS. In addition, according to the ratio between the numerical time step  $\Delta t$  and the cell-size-determined time step  $\Delta t_s$ , the temporal discretization for

**Table A.6**

Surface quantities along the upper wall at time  $t = 1.5$  for wall bounded Rayleigh flow at  $Kn = 0.05$ .

$x$	$p_w/\rho_0 C_0^2$	$\tau_w/\rho_0 C_0^2$	$q_w/\rho_0 C_0^3$
6.2111801e-03	5.3565e-01	1.2424e-02	7.4008e-02
1.3043478e-01	5.2399e-01	8.0181e-03	3.8776e-02
1.9254658e-01	5.2309e-01	7.0158e-03	3.0238e-02
2.7950310e-01	5.2275e-01	6.0035e-03	2.1583e-02
3.2919255e-01	5.2284e-01	5.5672e-03	1.7828e-02
3.7888199e-01	5.2306e-01	5.2149e-03	1.4741e-02
5.0310559e-01	5.2408e-01	4.6489e-03	9.3038e-03
5.7763975e-01	5.2488e-01	4.4971e-03	7.2490e-03
6.3975155e-01	5.2562e-01	4.4631e-03	6.0582e-03
6.8944099e-01	5.2620e-01	4.4889e-03	5.3808e-03
7.5155280e-01	5.2691e-01	4.5769e-03	4.8102e-03
8.7577640e-01	5.2797e-01	4.8808e-03	4.3264e-03
9.2546584e-01	5.2817e-01	5.0231e-03	4.2926e-03
9.5031056e-01	5.2820e-01	5.0930e-03	4.2963e-03
1.0000000e+00	5.2811e-01	5.2223e-03	4.3291e-03
1.0745342e+00	5.2754e-01	5.3644e-03	4.4000e-03
1.1366460e+00	5.2659e-01	5.4071e-03	4.4358e-03
1.1490683e+00	5.2635e-01	5.4052e-03	4.4371e-03
1.2484472e+00	5.2379e-01	5.2400e-03	4.3441e-03
1.3726708e+00	5.1929e-01	4.6358e-03	3.9138e-03
1.4968944e+00	5.1413e-01	3.6737e-03	3.1740e-03
1.6211180e+00	5.0932e-01	2.5718e-03	2.3075e-03
1.7453416e+00	5.0564e-01	1.5527e-03	1.5361e-03
1.8695652e+00	5.0342e-01	7.2076e-04	1.0193e-03
1.9937888e+00	5.0265e-01	3.2882e-05	8.2962e-04

**Table A.7**

Surface quantities along the lower wall at time  $t = 1.5$  for wall bounded Rayleigh flow at  $Kn = 0.05$ .

$x$	$p_w/\rho_0 C_0^2$	$\tau_w/\rho_0 C_0^2$	$q_w/\rho_0 C_0^3$
6.2111801e-03	4.9029e-01	3.2843e-03	6.2854e-02
1.3043478e-01	5.0831e-01	2.4156e-03	3.5665e-02
1.8012422e-01	5.1159e-01	2.2900e-03	2.9628e-02
2.2981366e-01	5.1413e-01	2.2386e-03	2.4683e-02
3.1677019e-01	5.1747e-01	2.2807e-03	1.7943e-02
3.7888199e-01	5.1931e-01	2.3864e-03	1.4290e-02
5.0310559e-01	5.2218e-01	2.7265e-03	9.1862e-03
6.2732919e-01	5.2442e-01	3.1866e-03	6.2751e-03
7.5155280e-01	5.2617e-01	3.7280e-03	4.8470e-03
8.7577640e-01	5.2730e-01	4.3004e-03	4.3391e-03
9.5031056e-01	5.2754e-01	4.6209e-03	4.2856e-03
1.0000000e+00	5.2746e-01	4.8070e-03	4.3023e-03
1.0745342e+00	5.2689e-01	5.0179e-03	4.3514e-03
1.1366460e+00	5.2597e-01	5.1075e-03	4.3727e-03
1.1614907e+00	5.2548e-01	5.1165e-03	4.3684e-03
1.2484472e+00	5.2325e-01	5.0104e-03	4.2670e-03
1.3726708e+00	5.1887e-01	4.4720e-03	3.8390e-03
1.4968944e+00	5.1384e-01	3.5658e-03	3.1145e-03
1.6211180e+00	5.0915e-01	2.5077e-03	2.2672e-03
1.7453416e+00	5.0555e-01	1.5192e-03	1.5121e-03
1.8695652e+00	5.0337e-01	7.0676e-04	1.0052e-03
1.9937888e+00	5.0261e-01	3.2270e-05	8.1898e-04

the implicit scheme has been improved. As a result, when the global numerical time step in IUGKS becomes as small as the one used in the explicit UGKS, the IUGKS can automatically recover the explicit method, where only one inner iteration for each step is needed. Based on numerical tests, the IUGKS has been validated in terms of accuracy, stability, computational efficiency. The IUGKS has second-order accuracy in both continuum and rarefied flow regimes. In general, the IUGKS is at least one order of magnitude more efficient than the explicit UGKS for unsteady flow computations. For the hypersonic rarefied flow, the IUGKS can obtain the time accurate solutions efficiently as well.

**Acknowledgement**

The work of Zhu and Zhong is supported by the National Natural Science Foundation of China (Grant No. 11472219), the National Pre-Research Foundation of China, and the 111 Project of China (B17037). The work of Zhu is also supported by

**Table A.8**Surface quantities alongside plate at time  $t = 1.5$  for wall bounded Rayleigh flow at  $Kn = 0.05$ .

$x$	$p_w / \rho_0 C_0^2$	$\tau_w / \rho_0 C_0^2$	$q_w / \rho_0 C_0^3$
6.1728395e-03	5.2104e-01	1.4074e-02	7.8678e-02
6.7901234e-02	5.2494e-01	9.6498e-03	6.4572e-02
1.2962963e-01	5.2408e-01	7.5477e-03	5.7702e-02
2.5308642e-01	5.2213e-01	5.5299e-03	5.0555e-02
3.7654321e-01	5.2128e-01	4.8126e-03	4.7414e-02
4.1358025e-01	5.2123e-01	4.7293e-03	4.6940e-02
4.8765432e-01	5.2142e-01	4.6716e-03	4.6508e-02
5.0000000e-01	5.2148e-01	4.6726e-03	4.6499e-02
5.7407407e-01	5.2208e-01	4.7215e-03	4.6822e-02
6.2345679e-01	5.2271e-01	4.7810e-03	4.7420e-02
7.4691358e-01	5.2534e-01	4.9456e-03	5.0643e-02
8.5802469e-01	5.2982e-01	5.0124e-03	5.7082e-02
9.4444444e-01	5.3636e-01	4.9719e-03	6.7810e-02
9.9382716e-01	5.4420e-01	5.0975e-03	8.2648e-02

the Excellent Doctorate Cultivating Foundation of Northwestern Polytechnical University. The current research is supported by the Hong Kong research grant council (16206617, 16207715) and NSFC (91530319, 11772281).

## References

- [1] Y. Zhu, C. Zhong, K. Xu, Implicit unified gas-kinetic scheme for steady state solutions in all flow regimes, *J. Comput. Phys.* 315 (2016) 16–38.
- [2] Y. Zhu, C. Zhong, K. Xu, Unified gas-kinetic scheme with multigrid convergence for rarefied flow study, *Phys. Fluids* 29 (9) (2017) 096102.
- [3] G.A. Bird, *Molecular Gas Dynamics and the Direct Simulation of Gas Flows*, Oxford University Press, USA, 1994.
- [4] L. Mieussens, Discrete-velocity models and numerical schemes for the Boltzmann-BGK equation in plane and axisymmetric geometries, *J. Comput. Phys.* 162 (2) (2000) 429–466.
- [5] L. Mieussens, Discrete velocity model and implicit scheme for the BGK equation of rarefied gas dynamics, *Math. Models Methods Appl. Sci.* 10 (08) (2000) 1121–1149.
- [6] Z.-H. Li, H.-X. Zhang, Study on gas kinetic unified algorithm for flows from rarefied transition to continuum, *J. Comput. Phys.* 193 (2) (2004) 708–738.
- [7] A.-P. Peng, Z.-H. Li, J.-L. Wu, X.-Y. Jiang, Implicit gas-kinetic unified algorithm based on multi-block docking grid for multi-body reentry flows covering all flow regimes, *J. Comput. Phys.* 327 (2016) 919–942.
- [8] K. Xu, J.-C. Huang, A unified gas-kinetic scheme for continuum and rarefied flows, *J. Comput. Phys.* 229 (20) (2010) 7747–7764.
- [9] J.-C. Huang, K. Xu, P. Yu, A unified gas-kinetic scheme for continuum and rarefied flows II: multi-dimensional cases, *Commun. Comput. Phys.* 12 (3) (2012) 662–690.
- [10] K. Xu, *Direct Modeling for Computational Fluid Dynamics: Construction and Application of Unified Gas-Kinetic Schemes*, World Scientific, Singapore, 2015.
- [11] Z. Guo, K. Xu, R. Wang, Discrete unified gas kinetic scheme for all Knudsen number flows: Low-speed isothermal case, *Phys. Rev. E* 88 (3) (2013) 033305.
- [12] Z. Guo, R. Wang, K. Xu, Discrete unified gas kinetic scheme for all Knudsen number flows. II. Thermal compressible case, *Phys. Rev. E* 91 (3) (2015) 033313.
- [13] S. Chen, K. Xu, A comparative study of an asymptotic preserving scheme and unified gas-kinetic scheme in continuum flow limit, *J. Comput. Phys.* 288 (2015) 52–65.
- [14] K. Xu, A gas-kinetic BGK scheme for the Navier–Stokes equations and its connection with artificial dissipation and Godunov method, *J. Comput. Phys.* 171 (1) (2001) 289–335.
- [15] S. Chen, K. Xu, C. Lee, Q. Cai, A unified gas kinetic scheme with moving mesh and velocity space adaptation, *J. Comput. Phys.* 231 (20) (2012) 6643–6664.
- [16] S. Liu, P. Yu, K. Xu, C. Zhong, Unified gas-kinetic scheme for diatomic molecular simulations in all flow regimes, *J. Comput. Phys.* 259 (2014) 96–113.
- [17] D. Jiang, *Study of the Gas-Kinetic Scheme Based on the Analytic Solution of Model Equations*, Ph.D. thesis, China Aerodynamics Research and Development Center, 2016.
- [18] J.-C. Huang, K. Xu, P. Yu, A unified gas-kinetic scheme for continuum and rarefied flows III: Microflow simulations, *Commun. Comput. Phys.* 14 (05) (2013) 1147–1173.
- [19] S. Liu, C. Zhong, J. Bai, Unified gas-kinetic scheme for microchannel and nanochannel flows, *Comput. Math. Appl.* 69 (1) (2015) 41–57.
- [20] K. Xu, C. Liu, A paradigm for modeling and computation of gas dynamics, *Phys. Fluids* 29 (2) (2017) 026101.
- [21] C. Liu, K. Xu, A unified gas-kinetic scheme for continuum and rarefied flows V: Multiscale and multi-component plasma transport, *Commun. Comput. Phys.* 22 (5) (2017) 1175–1223.
- [22] W. Sun, S. Jiang, K. Xu, S. Li, An asymptotic preserving unified gas kinetic scheme for frequency-dependent radiative transfer equations, *J. Comput. Phys.* 302 (2015) 222–238.
- [23] Z. Guo, K. Xu, Discrete unified gas kinetic scheme for multiscale heat transfer based on the phonon Boltzmann transport equation, *Int. J. Heat Mass Transf.* 102 (2016) 944–958.
- [24] A. Jameson, Time dependent calculations using multigrid, with applications to unsteady flows past airfoils and wings, *AIAA paper* 91-1596.
- [25] T. Pulliam, Time accuracy and the use of implicit methods, *AIAA paper* 93-3360.
- [26] R.F. Tomaro, W.Z. Strang, L.N. Sankar, An implicit algorithm for solving time dependent flows on unstructured grids, *AIAA paper* 97-0333.
- [27] S. Tan, Q. Li, Time-implicit gas-kinetic scheme, *Comput. Fluids* 144 (2017) 44–59.
- [28] J. Li, C. Zhong, Y. Wang, C. Zhuo, Implementation of dual time-stepping strategy of the gas-kinetic scheme for unsteady flow simulations, *Phys. Rev. E* 95 (5) (2017) 053307.
- [29] J. Yang, J. Huang, Rarefied flow computations using nonlinear model Boltzmann equations, *J. Comput. Phys.* 120 (2) (1995) 323–339.
- [30] M. Mao, D. Jiang, J. Li, X. Deng, Study on implicit implementation of the unified gas kinetic scheme, *J. Theor. Appl. Mech.* 47 (5) (2015) 822–829.
- [31] S. Jin, Asymptotic preserving (AP) schemes for multiscale kinetic and hyperbolic equations: a review, in: *Lecture Notes for Summer School on Methods and Models of Kinetic Theory (M&MKT)*, Porto Ercole (Grosseto, Italy), 2010, pp. 177–216.

- [32] W. Sun, S. Jiang, K. Xu, An implicit unified gas kinetic scheme for radiative transfer with equilibrium and non-equilibrium diffusive limits, *Commun. Comput. Phys.* 22 (4) (2017) 889–912.
- [33] W.T. Taitano, D.A. Knoll, L. Chacón, J.M. Reisner, A.K. Prinja, Moment-based acceleration for neutral gas kinetics with BGK collision operator, *J. Comput. Theor. Transp.* 43 (1–7) (2014) 83–108.
- [34] L. Chacon, G. Chen, D.A. Knoll, C. Newman, H. Park, W. Taitano, J.A. Willert, G. Womeldorff, Multiscale high-order/low-order (HOLO) algorithms and applications, *J. Comput. Phys.* 330 (2017) 21–45.
- [35] P. Degond, G. Dimarco, L. Pareschi, The moment-guided Monte Carlo method, *Int. J. Numer. Methods Fluids* 67 (2) (2011) 189–213.
- [36] A. Jameson, S. Yoon, Lower-upper implicit schemes with multiple grids for the Euler equations, *AIAA J.* 25 (7) (1987) 929–935.
- [37] S. Yoon, A. Jameson, Lower-upper symmetric-Gauss–Seidel method for the Euler and Navier–Stokes equations, *AIAA J.* 26 (9) (1988) 1025–1026.
- [38] L. Yuan, Comparison of implicit multigrid schemes for three-dimensional incompressible flows, *J. Comput. Phys.* 177 (1) (2002) 134–155.
- [39] Y. Saad, M.H. Schultz GMRES, A generalized minimal residual algorithm for solving nonsymmetric linear systems, *SIAM J. Sci. Stat. Comput.* 7 (3) (1986) 856–869.
- [40] C. Mouhot, L. Pareschi, Fast algorithms for computing the Boltzmann collision operator, *Math. Comput.* 75 (256) (2006) 1833–1852.
- [41] F. Filbet, C. Mouhot, L. Pareschi, Solving the Boltzmann equation in  $N \log_2 N$ , *SIAM J. Sci. Comput.* 28 (3) (2006) 1029–1053.
- [42] L. Wu, C. White, T.J. Scanlon, J.M. Reese, Y. Zhang, Deterministic numerical solutions of the Boltzmann equation using the fast spectral method, *J. Comput. Phys.* 250 (2013) 27–52.
- [43] L. Wu, J.M. Reese, Y. Zhang, Solving the Boltzmann equation deterministically by the fast spectral method: application to gas microflows, *J. Fluid Mech.* 746 (2014) 53–84.
- [44] C. Liu, K. Xu, Q. Sun, Q. Cai, A unified gas-kinetic scheme for continuum and rarefied flows IV: Full Boltzmann and model equations, *J. Comput. Phys.* 314 (2016) 305–340.
- [45] P.L. Bhatnagar, E.P. Gross, M. Krook, A model for collision processes in gases. I. Small amplitude processes in charged and neutral one-component systems, *Phys. Rev.* 94 (3) (1954) 511.
- [46] E. Shakhov, Generalization of the Krook kinetic relaxation equation, *Fluid Dyn.* 3 (5) (1968) 95–96.
- [47] R. Chen, Z. Wang, Fast, block lower-upper symmetric Gauss–Seidel scheme for arbitrary grids, *AIAA J.* 38 (12) (2000) 2238–2245.
- [48] H. Luo, J.D. Baum, R. Löhner, An accurate, fast, matrix-free implicit method for computing unsteady flows on unstructured grids, *Comput. Fluids* 30 (2) (2001) 137–159.
- [49] L. Pan, K. Xu, Q. Li, J. Li, An efficient and accurate two-stage fourth-order gas-kinetic scheme for the Euler and Navier–Stokes equations, *J. Comput. Phys.* 326 (2016) 197–221.
- [50] U. Trottenberg, C.W. Oosterlee, A. Schüller, *Multigrid*, Academic Press, 2001.
- [51] S. Chen, C. Zhang, L. Zhu, Z. Guo, A unified implicit scheme for kinetic model equations. Part I. Memory reduction technique, *Sci. Bull.* 62 (2) (2017) 119–129.